LIVERPOOL JOHN MOORES UNIVERSITY

Faculty Research Day

Wednesday

24th May 2023

Conference Papers

Rahma Abdulkadir

Postgraduate Researcher

School of Engineering

The dynamics of supply chain relationships on medicine availability: a case of Kaduna essential medicine delivery

R Abdulkadir, D B Matellini, I D Jenkinson, R Payne and T T Nguyen
School of Engineering, Liverpool John Moores University, Liverpool, United Kingdom
E-mail address: r.abdulkadir@2020.ljmu.ac.uk

Abstract. This study examines the relationships between medicine suppliers and the Kaduna State essential medicine supply chain to determine the dynamics of medicine procurement and on-shelf medicine availability. This study adopted a system dynamics perspective to explore the supply chain relationship between medicine suppliers and hospitals to reduce the lead time for medicine delivery and improve medicine fulfilment. In-depth semi-structured interviews were conducted with essential medicine manufacturers, distributors, and stakeholders to understand the relational dynamics that increase the availability of medicine. A simulation model was developed to test policies that improve network relationships to increase the medicine delivery speed and on-shelf availability. Increasing transparency using enterprise-wide systems for information, products, and cash flow between internal organisations and external suppliers improves collaboration and trust, leading to increased medicine availability within the network.

Keywords. Essential medicines, system dynamics, on-shelf availability, collaborative networks

1. Introduction

Healthcare supply chains engage multiple partners in delivering medicines to hospitals. Supply chain relationships and the ability to manage partners determine the success of interventions to increase the availability of on-shelf medicine (Kumar *et al.*, 2022). Kaduna State in Nigeria has been transforming the essential medicine supply chain to build better relationships with suppliers for the faster delivery of medicines to reduce stockouts. Coordinating complex supply chain partnerships to deliver medicines to over one thousand hospitals is a challenge that requires a systems approach to understand the dynamics of relational structures and behavioural feedbacks to improve on-shelf medicine availability (Abdulkadir *et al.*, 2023).

1.1. Supply chain relationships

Previous studies explored dyadic and triadic partnerships to improve performance (Wu *et al.*, 2010). Exploration of the benefits of transactional to collaborative partnerships has led procurement entities and suppliers to engage in co-creation activities for mutual benefits before initiating the tendering process (Holma *et al.*, 2020). Studies have called for examining factors that increase trust and partnership commitments from a multi-stakeholder viewpoint, taking into consideration the need for seamless information flows across supply chains (Tsanos and Zografos, 2016). As healthcare supply chains continue to struggle to provide medicines for patient care, suppliers encounter challenges with the production and delivery of products at the right time (Kumar *et al.*, 2022). Some studies have examined how organisations can build relationships backed by technology to increase trust and transparency. Although technology enables information flow and increases transparency in the system, the behaviour of actors towards the use of these innovative technologies might hinder adoption (Giri and Manohar, 2023). This research aims to fill the gaps in previous studies by examining the dynamic relational capacity of essential medicine delivery from a multi-stakeholder perspective and extending the boundaries of supply chains to include critical stakeholders such as third-party service providers,

manufacturers, and wholesalers. Building relational capacity helps managers work well with multiple stakeholders to improve on-shelf medicine availability and reduce stockouts.

2. Methodology

A stock-and-flow model was developed from the six in-depth interview variables elicited from Essential Medicine Managers (EMM), Manufacturer (M), Wholesaler (W), Drone Logistics Provider (DLP), and International Donor Organisation (IDO) (Table 1). The model was developed using a system dynamics distribution model (Sterman, 2000). All participants had over 10 years of experience in operating an essential medicine program. Interviewees were selected based on criterion sampling. Two participants were managers in the organisations, while four participants were partners to the focal organisation (FO).

Table 1: Multi-stakeholder interview participants in the essential medicine program.

Participants' category	Number of interviewees
Essential medicine managers	2
Manufacturer	1
Wholesaler	1
Drone logistics provider	1
International donor organisation	1

3. Internal and boundary spanning collaboration variables

The findings from the study showed that four types of trust loops in the system drive behaviour towards collaboration. These loops include FO-teamwork, FO-customer relationships, FO-stakeholder relationships, and FO-supplier relationships. Variables affecting trust, together with closely linked variables of internal and supplier performance, stakeholder, and customer satisfaction, must be considered when developing policies to increase the on-shelf availability of essential medicines (Table 2).

Table 2: Trust variables driving collaboration across the focal organisation supply chain.

Internal collaboration variables	Percentage of interviewees identifying Internal collaboration variables (%)	Boundary spanning collaboration variables	Percentage of interviewees identifying boundary spanning variables (%)
Teamwork	33%	FO-customer relationship	17%
Transparency	50%	FO-stakeholder relationship	33%
Visibility	100%	FO-supplier relationship	50%
Performance	17%	Transparency	50%
Information sharing	100%	Visibility	100%
Communication	83%	Supplier performance	17%
		Information sharing	100%
		Stakeholder satisfaction	17%
		Collaboration	67%
		Customer satisfaction	17%
		Communication	83%
		Strategic alliance	17%
		Wholesaler-manufacturer relationship (trust)	17%
		Wholesaler-FO Relationship (trust)	17%
		Process integration	50%

3.1. Tragedy of unplanned procurement

The use of data for decision-making reduces the need for emergency and unplanned procurement, thereby stabilising the system to avoid the tragedy of unplanned procurement, where nobody wins and stakeholder satisfaction is eroded over time (figure 1). FO receives emergency orders from hospitals and procures medicines from wholesalers and manufacturers to deliver medicines to hospitals on time. Although emergency procurement is faster, it destabilises the systems, as suppliers are also under pressure to deliver under uncertain conditions. Because of the large number of hospitals receiving essential medicines from the FO, the need to provide suppliers with visibility which is currently absent in the system will reduce the procurement planning time, because the use of accurate data will enable suppliers to plan for delivery and fulfilment to all hospitals. Adequate planning reduces waste from overstocking medicine, which can lead to expiries.

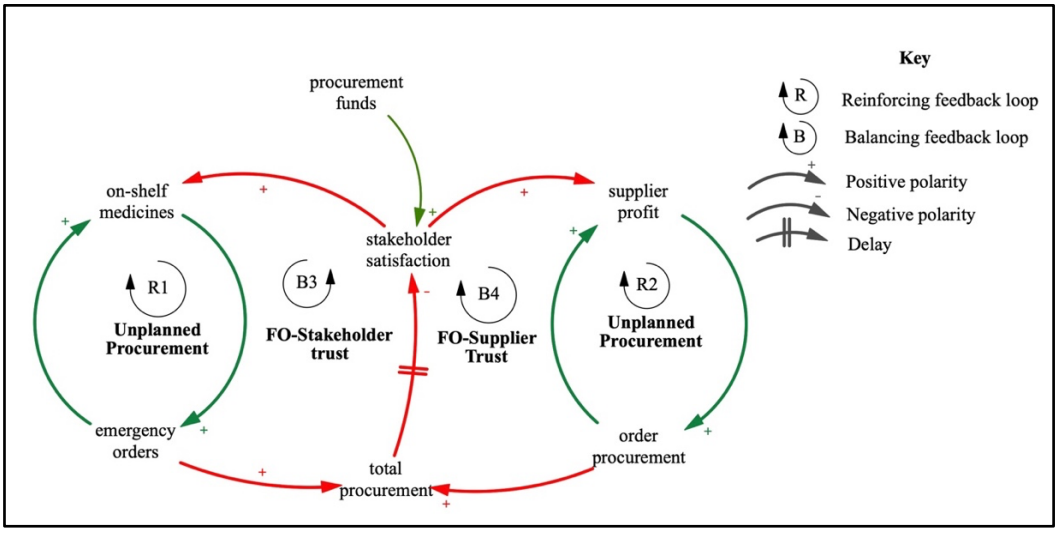

Figure 1: Tragedy of unplanned procurement across the focal organisation's supply chain.

4. Policies for improving trust and collaboration

Reducing expiries increase on-shelf medicines and stakeholder trust which leads to an increase in the on-shelf fill rate (figure 2). The baseline scenario starts with a 9% medicine expiry at baserun, with an on-shelf fill rate of 17% and 23% trust among stakeholders. When expiries reduced to 1%, stakeholder trust increased to 97% and on-shelf fill rate increased to 96%.

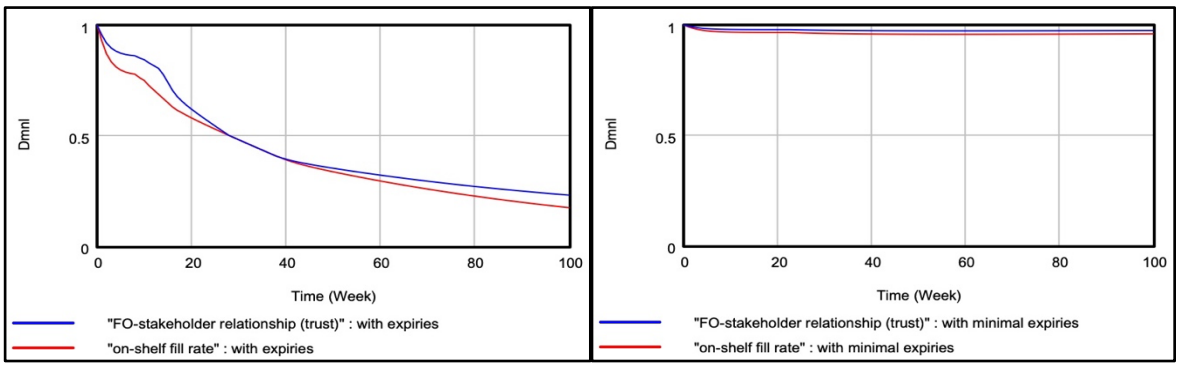

(a) (b)

Figure 2: Effect of expiries on stakeholder trust and on-shelf fill rate at baseline (a) and with minimal expiries (b).

FO uses data collection and enterprise resource planning tools to determine the quantity of medicines shipped to hospitals, but visibility from the hospital is partial. Suppliers do not have access to hospital orders. There is a need to integrate all tools into one system for upstream and downstream information sharing. The use of instant drone technologies by FO can be extended to its partners, and medicine delivery can be restructured to include vendor-managed distribution (VMD) for specific categories of products. VMD reduces inventory holding and transportation costs to the FO warehouse. The orders received by FO can be delivered directly to hospitals. Instant delivery minimises delays from poor road networks and security challenges, leading to higher on-shelf availability.

4.1. Minimising unplanned procurement

Policies to minimise unplanned procurement include joint planning with suppliers and stakeholders to consider all factors during essential medicine forecasting, replenishment, and delivery. Continuous sales and operations planning with suppliers and DLP improves the shared understanding of the relational factors leading to on-shelf availability. FO can benefit from the knowledge reservoir of suppliers as the diffusion of information closes the knowledge gap in the supply chain.

5. Conclusions and recommendation

FO should integrate its technology platforms with suppliers and DLP for an adequate supply plan and distribution of essential medicines. Manufacturers and wholesalers can benefit from drone logistics services to increase the delivery rate and scale. Collaborative relationships expand the benefits for each stakeholder to save costs and reduce lead-times. This study recommends that the government design collaborative policies that support multi-stakeholder relationship building backed by technology to increase transparency and trust in the supply chain. The structural design of public health supply chains must integrate manufacturers, wholesalers, and other service delivery partners to deliver lifesaving medicines effectively. The FO-DLP partnership can serve as a boundary-spanning integrator for government and private sector collaborative supply chain programmes.

Acknowledgments

I wish to acknowledge the financial support provided by the Kühne Foundation for completing this study.

References

Abdulkadir, R., Matellini, D. B., Jenkinson, I. D., Pyne, R. and Nguyen, T. T. (2023) 'Assessing performance using maturity model: a multiple case study of public health supply chains in Nigeria', *Journal of Humanitarian Logistics and Supply Chain Management*. https://doi.org/10.1108/jhlscm-05-2022-0053.

Giri, G., and Manohar, H. L. (2023) 'Factors influencing the acceptance of private and public blockchain-based collaboration among supply chain practitioners: a parallel mediation model', *Supply Chain Management: An International Journal*, 28(1), pp. 1-24. https://doi.org/10.1108/scm-02-2021-0057.

Holma, A. M., Vesalainen, J., Söderman, A., Sammalmaa, J. (2020) 'Service specification in pre-tender phase of public procurement - A triadic model of meaningful involvement', *Journal of Purchasing and Supply Management*, 26(1), p. 100580. https://doi.org/10.1016/j.pursup.2019.100580.

Kumar, V., Ya, K. Z. and Lai, K. K. (2022) 'Mapping the key challenges and managing the opportunities in supply chain distribution during COVID-19: a case of Myanmar pharmaceutical company', *Journal of Global Operations and Strategic Sourcing*. https://doi.org/10.1108/jgoss-01-2022-0002.

Sterman, J. (2000) *Business Dynamics: Systems Thinking and Modeling for a Complex World*. McGraw-Hill, New York.

Tsanos, C. S. and Zografos, K. G. (2016) 'The effects of behavioural supply chain relationship antecedents on integration and performance', *Supply Chain Management-an International Journal*, 21(6), pp. 678-693.

Wu, Z., Choi, T. Y. and Rungtusanatham, M. J. (2010) 'Supplier–supplier relationships in buyer–supplier–supplier triads: Implications for supplier performance', *Journal of Operations Management*, 28(2), pp. 115-123.

Thibaut Galvain

Postgraduate Researcher

School of Computer Science and Mathematics

The management of anticoagulants in patients with atrial fibrillation and history of falls or risk of falls: The Liverpool AF-Falls Project. A systematic review and multilevel meta-analysis

Thibaut Galvain[1], Ruaraidh Hill[2], Sarah Donegan[3], Paulo Lisboa[4], Gregory Y. H. Lip[5] and Gabriela Czanner[6]

[1.] School of Computer Science and Mathematics, Liverpool John Moores University, Liverpool, UK.

[2.] Reviews And Implementation Group, Health Data Science, University of Liverpool and The Royal Liverpool and Broadgreen University Hospitals, Liverpool Health Partners, Liverpool, UK

[3.] Department of Health Data Science, University of Liverpool, Liverpool, UK

[4.] School of Computer Science and Mathematics, Liverpool John Moores University, Liverpool, UK.

[5.] Liverpool Centre for Cardiovascular Science, University of Liverpool and Liverpool Heart and Chest Hospital, Liverpool, United Kingdom

[6.] School of Computer Science and Mathematics, Liverpool John Moores University, Liverpool, UK; and Faculty of Informatics and Information Technologies, Slovak University of Technology, Slovakia.

Corresponding author: Thibaut Galvain, School of Computing and Mathematical Science, Liverpool John Moores University, Liverpool, UK; Email: t.galvain@2019.ljmu.ac.uk

Abstract

Background: Atrial fibrillation (AF) is a major cause of stroke. Anticoagulants substantially reduce risk of stroke but are also associated with an increased risk of bleeding. This systematic review and meta-analysis aims to compare anticoagulant treatment options for the management of atrial fibrillation patients at risk of falls or with a history of falls.

Methods: We conducted a PRISMA systematic review (until March 2022), including studies evaluating safety and efficacy of different anticoagulants (Vitamin K antagonist [VKA] versus non-vitamin K antagonist oral anticoagulant [NOAC]). A multilevel meta-analysis was conducted adjusting for clustering effects within studies examining more than one effect size.

Results: 919 articles were identified, 155 were screened for full text and 10 articles were retained for final quantitative synthesis. Risk of bias was moderate to serious for the included studies. In meta-analysis, NOACs were associated with superior effectiveness compared to VKA for ischemic stroke/systemic embolism (HR 0.82, 95%CI [0.69–0.98]; p<0,05) and safety (hazard ratio (HR) 0.53, 95% confidence interval (CI) [0.40–0.71]; p<0,05) for intracranial hemorrhage. There were no differences in other outcomes.

Conclusion: NOACs were associated with less intracranial haemorrhages and ischemic strokes/systemic embolisms than VKAs in AF patients at risk of falls.

Keywords: Systematic review, meta-analysis, VKA, NOAC, falls, Atrial fibrillation, anticoagulant

1. Introduction

Atrial fibrillation (AF) is the most common sustained cardiac arrhythmia (1) and is a major cause of stroke, heart failure, and death (2), as well as healthcare costs (3). Stroke is the second most common cause of death and it is a major cause of disability (4). AF patients have a yearly risk of stroke of 5%, and this risk is increased in the presence of certain risk factors, including left ventricular dysfunction, hypertension, a history of stroke, and increasing age (5).

Treatment with oral anticoagulants (OACs) substantially reduces risk of stroke but are also associated with an increased risk of bleeding and especially intracranial haemorrhages which are the most feared complication (6,7). Because of that, many patients do not receive anticoagulants, and particularly patients at risk of falls or with history of falls (8,9). AF patients at high risk of falls and on oral anticoagulation do not have a significantly increased risk of major bleeding, suggesting that being at risk of falls should not prevent OAC prescribing (10,11).

The non-vitamin K antagonist oral anticoagulants (NOACs) were shown in a number of systematic reviews and meta-analyses to reduce the risk for intracranial hemorrhage by approximately 50% compared with vitamin K antagonists (VKAs) in the general AF population at risk of stroke (12,13), and are therefore the preferred option in guidelines (14,15). NOACs might be the most appropriate anticoagulant in patients with an increased risk of falls and help to alleviate fears of bleeding complications.

To our knowledge there is limited evidence and there are no recommendations and guidelines for the use of NOACs specifically for the patients at risk of falls or with history of falls. In the first contemporary study of its kind, the Liverpool AF-Falls project aims to determine the safety and efficacy of NOACs compared with vitamin K antagonists (VKAs) for the management of AF patients at risk of falls or with a history of falls. Results from the project could provide clinicians and policy makers with information on which to make evidence-based recommendations.

2. Methods

Randomized controlled trials (RCT) (including *post hoc* and ancillary analysis), quasi-randomized studies and observational (prospective, retrospective, case control and cohort studies) studies were included. We included studies of adults (age 18 or older) patients with any forms of nonvalvular AF (paroxysmal, persistent or permanent) with history of falls or that are at risk of falls comparing NOACs to VKAs. Patients were defined at risk of falls if they had one of these criteria based on a revised list from Steffel *et al.*(16): prior history of falls; lower extremity weakness; poor balance; cognitive impairment; vision and/or hearing impairment; orthostatic hypotension; use of psychotropic or antihistaminic, or anticholinergic, or antihypertensive drugs; severe arthritis; dizziness; frailty; polypharmacy defined as a minimum of six pharmaceutical treatments and multimorbidity defined as a minimum of four comorbidities.

The primary efficacy outcome was the composite of ischemic stroke and/or systemic embolism (an acute vascular occlusion of an extremity or organ). The primary safety outcome was major bleeding. Secondary outcomes included: intracranial haemorrhage (Including all intracerebral, subdural, epidural, subarachnoid haemorrhage and haemorrhagic stroke); gastrointestinal bleeding; clinically relevant non-major bleeding; myocardial infarction; ischemic stroke; systemic embolism; haemorrhagic stroke; cardiovascular mortality and all-cause mortality.

The following bibliographic databases were searched: Cochrane Central Register of Controlled Trials (CENTRAL), CINAHL, Embase (via OVID); MEDLINE (via OVID), Scopus and Web of Science. We also searched the following trials register: the US National Institutes of Health Register (www.clinicaltrials.gov). English-language articles published from inception to March 2022 were identified.

Two independent reviewers (TG and GC) performed study selection. During stage 1, titles and abstracts were screened to identify potentially relevant studies applying the inclusion and exclusion criteria. At stage 2, full-text review established the final set of included studies, with discrepancies resolved by a third reviewer (GL). In this systematic review, risk of bias in observational studies was appraised with the Risk Of Bias In Non-randomized Studies - of Interventions I tool (ROBINS-I tool) (17).

Data synthesis was conducted based on the sufficient clinical homogeneity regarding participant characteristics, types of intervention and outcomes, and comparability between methods and ability to aggregate data. Statistical heterogeneity as consequence of clinical and/or methodological diversity

was evaluated both by visual inspection of the forest plots and a formal statistical test, using Cochran Q test and I^2 statistic (18). If heterogeneity was low or minor, a fixed effect model was used to pool the data; if heterogeneity was moderate-to-substantial a random-effects model was use instead.(18) For the fixed effect model, the generic inverse variance method was used. For the random-effects model, data was pooled across studies using the DerSimonian and Laird model (19).

For outcomes that included studies with multiple effect sizes (e.g., when a study provided separate effect sizes for different NOACs, or different subgroups of patients being at risk of falls) a multilevel random effects meta-analysis was conducted which takes into account the hierarchical structure of the dataset (20,21). We assumed that effect sizes within studies were correlated with a correlation coefficient $\rho=0.5$ to calculate the variance-covariance matrix (sensitivity analyses were conducted using $\rho=0.3$ and $\rho=0.7$) (21,22). The restricted maximum likelihood method was used to estimate model overall effect. Confidence intervals of the model coefficients were calculated with robust variance estimation (23). Results of meta-analysis were presented as pooled HRs with 95% CIs.

3. Results

During the search process, 919 abstracts were identified. Following the removal of duplicates, 693 abstracts were excluded at stage 1, 155 full-text articles were assessed further for eligibility, and 10 met eligibility criteria for inclusion in this review. All studies were non-randomized. Five articles were retrospective cohorts (24–28), and the others were subgroup analyses of randomized clinical trials (one pre-specified subgroup analysis of ENGAGE-AF-TIMI trial (16,29), three post-hoc analyses of the ARISTOTLE trial (30–33) and one post-hoc analysis of the ROCKET AF trial (34,35)). Lip *et al.* 2020 (26), Hohmann *et al.* 2019 (28) and Martinez *et al.* 2018 (27) contributed three effect sizes each as they investigated either different NOACs compared to VKA, or different subgroups of AF patients being at risk of falls. The subgroup analyses (30–32) of the ARISTOTLE trial also contributed three effect sizes as they analysed distinctly different subgroups of AF patients being at risk of falls. Sample sizes ranged between 617 and 79,796 AF patients at moderate or high thromboembolic risk and with history of falls (30) or at risk of falls (16,24–28,31,32,34). Based upon the ROBINS-I tool for non-randomized studies, the overall risk of bias ranged from moderate to serious according to the included articles.

In the prophylaxis of stroke or systemic embolism (15 effect sizes), NOACS were superior to VKAs (hazard ratio (HR) 0.82, 95% confidence interval (CI) [0.69–0.98]; $p<0.05$; $I^2=67.7\%$)). Of the 10 articles included in the meta-analysis, seven evaluated the hazard for intracranial haemorrhage (15 effect sizes), which was lower with NOACs compared to VKA (HR 0.53, 95%CI [0.40–0.71]; $p<0,05$; $I^2=46\%$). In reducing the risk of major bleeding (11 effect sizes), NOACs were not different from VKAs (HR 0.88, 95%CI [0.74–1.04]; p=0.09). There were no differences between NOACs and VKA regarding risks in ischemic stroke (HR 0.87, 95%CI [0.60-1.28], p=0.23; eight effect sizes), haemorrhagic stroke (HR 0.51, 95%CI [0.24–1.10]; p=0.10; nine effect sizes), gastro-intestinal bleeding (HR 1.04, 95%CI [0.89-1.23], p=0.44; 12 effect sizes), myocardial infarction (HR 0.76, 95%CI [0.47-1.24], p=0.27; fixed effect model, reported in two studies), cardiovascular mortality (HR 1.04, 95%CI [0.61–1.75]; p=0.89; random effect model, reported in two studies) and all-cause mortality (HR 1.23, 95%CI [0.35–4.29]; p=0.55; five effect sizes). Sensitivity analyses results were aligned with the main results, regardless of the outcomes, for a correlation coefficient $\rho=0.3$ or $\rho=0.7$.

4. Discussion

This systematic review and meta-analysis of 10 studies is the first to compare NOACs with VKAs as anticoagulation strategies for patients with non-valvular atrial fibrillation and at risk of falls or with history of falls. The main findings from the pooled analyses were as follows: (1) there was a 18% reduction in the risk of stroke or systemic embolism with NOACs compared to VKAs and a 47% reduction in the risk of intracranial haemorrhage. (2) The risk of major bleeding events is not different between groups, as were the risks for ischemic stroke, haemorrhagic stroke, gastro-intestinal bleeding, myocardial infarction, cardiovascular and all-cause mortality.

Given the modest improvement of NOACs in preventing thromboembolic events such as stroke or systemic embolism compared to VKA, the safety of each treatment is of paramount importance and must be rigorously considered to decide the most appropriate antithrombotic management. We found in our meta-analysis found a 47% reduction in the risk of intracranial haemorrhage with NOACs as compared with VKAs. The shorter half-life of NOACs and the more targeted mechanism of anticoagulation (direct thrombin or factor Xa inhibition) have been implicated in the reduction of intracranial haemorrhage with these agents as compared with VKAs (29). The 2014 AHA/ACC/HRS Guideline for the Management of Patients With Atrial Fibrillation does not make specific recommendations for use of anticoagulation in AF patients at risk of falls or with history of falls (36). The present meta-analysis adds to the body of evidence suggesting that NOACs may be the optimal strategy for antithrombotic management, given the improved efficacy in preventing thromboembolic events and the improved safety profile as compared with VKAs.

This study has limitations. In particular, the included studies were not randomized; five studies were retrospective, and the others were subgroup analyses of randomized clinical trials (one pre-specified and four post-hoc). To investigate the effect of differential baseline prognosis between interventions, subgroup analyses were planned but could not be conducted due to the limited sample size. Similarly, we could not conduct a moderator analysis according to the different NOACs used but also due to the fact that some studies did not specify which NOAC was considered or did not stratify the results. There was also some variation in the definition of risk of falls used by different studies. Although these definitions were similar in according to our pre-specified protocol, we cannot exclude the possibility that standardized population definitions would have led to different results. Finally, due to the limited number of studies included, this systematic literature review and meta-analysis may still be underpowered to detect small but significant bleeding or thrombotic differences between VKAs and NOACs.

Our study has several strengths. It is the first to provide an up-to-date synthesis of the available literature in a dynamically evolving field and focusing on patients at risk of falls or with history of falls which have been underrepresented in the RCTs. Second, this study presents robust evidence on the comparative effectiveness and safety of NOACs compared to VKAs including the use of real world data which are more representative of patients being treated with anticoagulants in clinical practice. Third, it uses the latest development in meta-analysis methods in the presence of dependency, overcoming the limitations from the other methods suggested in Cochrane Handbook in the presence of multi-arm studies (21). These methods enable the use of all available effect sizes in the analyses, so all information can be preserved and maximum statistical power is achieved (22). Finally, we used the ROBINS-I tool to evaluate the quality of the included studies, tools that enable a robust assessment of the risk of different biases such as confounding or selection bias. This multilevel meta-analysis highlighted the superiority of NOACs in terms of safety and efficacy compared with VKAs in AF patients at risk of falls or with history of falls. Further research should be conducted to evaluate which NOAC should be preferred in this patient population, using network meta-analysis methods.

5. Conclusions

Our systematic review and multilevel meta-analysis suggest that NOACs are reducing the risk of ischemic stroke or systemic embolism (-18%) and intracranial haemorrhage (-47%) compared to VKAs in patients with AF and at risk or with history of falls. There were no major differences in the risks of major bleeding, ischemic stroke, haemorrhagic stroke, gastro-intestinal bleeding, cardiovascular and all-cause mortality.

6. References

1. Markides V, Schilling RJ. Atrial fibrillation: classification, pathophysiology, mechanisms and drug treatment. Heart. 2003 Aug;89(8):939–43.

2. Chugh SS, Havmoeller R, Narayanan K, Singh D, Rienstra M, Benjamin EJ, et al. Worldwide epidemiology of atrial fibrillation: a Global Burden of Disease 2010 Study. Circulation. 2014 Feb 25;129(8):837–47.
3. Burdett P, Lip GYH. Atrial fibrillation in the UK: predicting costs of an emerging epidemic recognizing and forecasting the cost drivers of atrial fibrillation-related costs. European Heart Journal - Quality of Care and Clinical Outcomes. 2022 Mar 2;8(2):187–94.
4. Marini C, De Santis F, Sacco S, Russo T, Olivieri L, Totaro R, et al. Contribution of atrial fibrillation to incidence and outcome of ischemic stroke: results from a population-based study. Stroke. 2005 Jun;36(6):1115–9.
5. Risk Factors for Stroke and Efficacy of Antithrombotic Therapy in Atrial Fibrillation: Analysis of Pooled Data From Five Randomized Controlled Trials. Archives of Internal Medicine. 1994 Jul 11;154(13):1449.
6. Staerk L, Sherer JA, Ko D, Benjamin EJ, Helm RH. Atrial Fibrillation: Epidemiology, Pathophysiology, and Clinical Outcomes. Circ Res. 2017 Apr 28;120(9):1501–17.
7. Katsanos AH, Schellinger PD, Köhrmann M, Filippatou A, Gurol ME, Caso V, et al. Fatal oral anticoagulant-related intracranial hemorrhage: a systematic review and meta-analysis. Eur J Neurol. 2018;25(10):1299–302.
8. Kakkar AK, Mueller I, Bassand JP, Fitzmaurice DA, Goldhaber SZ, Goto S, et al. Risk profiles and antithrombotic treatment of patients newly diagnosed with atrial fibrillation at risk of stroke: perspectives from the international, observational, prospective GARFIELD registry. PLoS ONE. 2013;8(5):e63479.
9. Bahri O, Roca F, Lechani T, Druesne L, Jouanny P, Serot JM, et al. Underuse of oral anticoagulation for individuals with atrial fibrillation in a nursing home setting in France: comparisons of resident characteristics and physician attitude. J Am Geriatr Soc. 2015;63(1):71–6.
10. Donzé J, Clair C, Hug B, Rodondi N, Waeber G, Cornuz J, et al. Risk of falls and major bleeds in patients on oral anticoagulation therapy. Am J Med. 2012;125(8):773–8.
11. Man-Son-Hing M, Nichol G, Lau A, Laupacis A. Choosing antithrombotic therapy for elderly patients with atrial fibrillation who are at risk for falls. Arch Intern Med. 1999 Apr 12;159(7):677–85.
12. Caldeira D, Barra M, Pinto FJ, Ferreira JJ, Costa J. Intracranial hemorrhage risk with the new oral anticoagulants: a systematic review and meta-analysis. J Neurol. 2015 Mar;262(3):516–22.
13. Hicks T, Stewart F, Eisinga A. NOACs versus warfarin for stroke prevention in patients with AF: a systematic review and meta-analysis. Open Heart. 2016 Jan;3(1):e000279.
14. Chao TF, Joung B, Takahashi Y, Lim TW, Choi EK, Chan YH, et al. 2021 Focused Update Consensus Guidelines of the Asia Pacific Heart Rhythm Society on Stroke Prevention in Atrial Fibrillation: Executive Summary. Thromb Haemost. 2022 Jan;122(01):020–47.
15. Hindricks G, Potpara T, Dagres N, Arbelo E, Bax JJ, Blomström-Lundqvist C, et al. 2020 ESC Guidelines for the diagnosis and management of atrial fibrillation developed in collaboration with the European Association for Cardio-Thoracic Surgery (EACTS). European Heart Journal. 2021 Feb 1;42(5):373–498.
16. Steffel J, Giugliano RP, Braunwald E, Murphy SA, Mercuri M, Choi Y, et al. Edoxaban Versus Warfarin in Atrial Fibrillation Patients at Risk of Falling: ENGAGE AF–TIMI 48 Analysis. Journal of the American College of Cardiology. 2016 Sep 13;68(11):1169–78.
17. Sterne JA, Hernán MA, Reeves BC, Savović J, Berkman ND, Viswanathan M, et al. ROBINS-I: a tool for assessing risk of bias in non-randomised studies of interventions. BMJ. 2016 Oct 12;i4919.
18. Higgins JPT, Thompson SG, Deeks JJ, Altman DG. Measuring inconsistency in meta-analyses. BMJ. 2003 Sep 6;327(7414):557–60.
19. DerSimonian R, Laird N. Meta-analysis in clinical trials. Control Clin Trials. 1986 Sep;7(3):177–88.
20. Assink M, Wibbelink CJM. Fitting three-level meta-analytic models in R: A step-by-step tutorial. TQMP. 2016 Oct 1;12(3):154–74.
21. Higgins JP, Eldridge S, Li T. Including variants on randomized trials. In: Higgins JPT, Thomas J, Chandler J, Cumpston M, Li T, Page MJ, et al., editors. Cochrane Handbook for Systematic

Reviews of Interventions [Internet]. 1st ed. Wiley; 2019 [cited 2022 Apr 21]. p. 569–93. Available from: https://onlinelibrary.wiley.com/doi/10.1002/9781119536604.ch23
22. Pustejovsky J, Tipton E. Meta-analysis with Robust Variance Estimation: Expanding the Range of Working Models. Prevention Science. 2021;
23. Pustejovsky JE, Tipton E. Small-Sample Methods for Cluster-Robust Variance Estimation and Hypothesis Testing in Fixed Effects Models. Journal of Business & Economic Statistics. 2018 Oct 2;36(4):672–83.
24. Miao B, Alberts MJ, Bunz TJ, Coleman CI. Safety and effectiveness of oral factor Xa inhibitors versus warfarin in nonvalvular atrial fibrillation patients at high-risk for falls. J Thromb Thrombolysis. 2019;48(3):366–72.
25. Fanning L, Lau WCY, Mongkhon P, Man KKC, Bell JS, Ilomäki J, et al. Safety and Effectiveness of Direct Oral Anticoagulants vs Warfarin in People With Atrial Fibrillation and Dementia. Journal of the American Medical Directors Association. 2020 Aug;21(8):1058-1064.e6.
26. Lip GYH, Keshishian AV, Kang AL, Dhamane AD, Luo X, Li X, et al. Oral anticoagulants for nonvalvular atrial fibrillation in frail elderly patients: insights from the ARISTOPHANES study. J Intern Med. 2021 Jan;289(1):42–52.
27. Martinez BK, Sood NA, Bunz TJ, Coleman CI. Effectiveness and Safety of Apixaban, Dabigatran, and Rivaroxaban Versus Warfarin in Frail Patients With Nonvalvular Atrial Fibrillation. JAHA. 2018 Apr 17;7(8):e008643.
28. Hohmann C, Hohnloser SH, Jacob J, Walker J, Baldus S, Pfister R. Non-Vitamin K Oral Anticoagulants in Comparison to Phenprocoumon in Geriatric and Non-Geriatric Patients with Non-Valvular Atrial Fibrillation. Thromb Haemost. 2019 Jun;119(06):971–80.
29. Giugliano RP, Ruff CT, Braunwald E, Murphy SA, Wiviott SD, Halperin JL, et al. Edoxaban versus Warfarin in Patients with Atrial Fibrillation. New England Journal of Medicine. 2013 Nov 28;369(22):2093–104.
30. Rao MP, Vinereanu D, Wojdyla DM, Alexander JH, Atar D, Hylek EM, et al. Clinical Outcomes and History of Fall in Patients with Atrial Fibrillation Treated with Oral Anticoagulation: Insights From the ARISTOTLE Trial. Am J Med. 2018;131(3):269-275.e2.
31. Jaspers Focks J, Brouwer MA, Wojdyla DM, Thomas L, Lopes RD, Washam JB, et al. Polypharmacy and effects of apixaban versus warfarin in patients with atrial fibrillation: post hoc analysis of the ARISTOTLE trial. BMJ. 2016 Jun 15;i2868.
32. Alexander KP, Brouwer MA, Mulder H, Vinereanu D, Lopes RD, Proietti M, et al. Outcomes of apixaban versus warfarin in patients with atrial fibrillation and multi-morbidity: Insights from the ARISTOTLE trial. American Heart Journal. 2019 Feb;208:123–31.
33. Granger CB, Alexander JH, McMurray JJV, Lopes RD, Hylek EM, Hanna M, et al. Apixaban versus Warfarin in Patients with Atrial Fibrillation. New England Journal of Medicine. 2011 Sep 15;365(11):981–92.
34. Piccini JP, Hellkamp AS, Washam JB, Becker RC, Breithardt G, Berkowitz SD, et al. Polypharmacy and the Efficacy and Safety of Rivaroxaban Versus Warfarin in the Prevention of Stroke in Patients With Nonvalvular Atrial Fibrillation. Circulation. 2016 Jan 26;133(4):352–60.
35. Patel MR, Mahaffey KW, Garg J, Pan G, Singer DE, Hacke W, et al. Rivaroxaban versus warfarin in nonvalvular atrial fibrillation. N Engl J Med. 2011 Sep 8;365(10):883–91.
36. January CT, Wann LS, Alpert JS, Calkins H, Cigarroa JE, Cleveland JC, et al. 2014 AHA/ACC/HRS Guideline for the Management of Patients With Atrial Fibrillation: A Report of the American College of Cardiology/American Heart Association Task Force on Practice Guidelines and the Heart Rhythm Society. Journal of the American College of Cardiology. 2014 Dec 2;64(21):e1–76.

Andrew Mason

Postgraduate Researcher

Astrophysics Research Institute

The anatomy of the knee: is there a strong relation between $[\mathrm{Fe/H}]_{\mathrm{knee}}$ and the stellar mass of galaxies?

A C Mason, R P Schiavon, R A Crain
Astrophysics Research Institute, Liverpool John Moores University
146 Brownlow Hill, Liverpool, L3 5RF
E-mail address: A.C.Mason@2015.ljmu.ac.uk

Abstract. The stars of Local Group dwarf galaxies are typically distributed in the [α/Fe]-[Fe/H] plane in the form of a high-α plateau at low [Fe/H] connected to a sequence of declining [α/Fe] at higher [Fe/H] by a so-called 'α knee'. Models of galactic chemical evolution suggest that these features are a consequence of extended histories of star formation, and that the 'α-knee' is caused by the different enrichment timescales of core-collapse supernovae (CCSNe) and Type Ia supernovae (SNe Ia). We test this hypothesis in a cosmological setting by examining the chemical compositions of over 1,000 galaxies in a high-resolution realisation of the EAGLE simulations. The subset of the galaxy population that shows knees exhibits a positive correlation between stellar mass and knee metallicity whose slope and pronounced scatter at fixed $M_\star$ are consistent with that which has been observed in Local Group galaxies.

Keywords. galaxies:abundances – galaxies:dwarf – galaxies: stellar content – galaxies:Local Group – galaxies:evolution –galaxies:general

1. Introduction

The field of Galactic archaeology-- the study of the properties of resolved fossil stellar populations of the Milky Way--has been transformed by a number of recent technological advancements which ushered in the era of massive stellar surveys. Precision element abundances and phase space properties of millions of stars can now be measured and interpreted within the broader context of theoretical predictions from galaxy formation theory to help elucidate the formation history of the Galaxy.

The stars of the dwarf galaxies inhabiting the Local Group are attractive targets for spectroscopic surveys, hosting both `fossil' and young stellar populations. The Milky Way occupies a unique position as a disk galaxy with potentially unusual properties [1] which means that its study alone is incapable of producing an all-encompassing picture of galaxy formation and evolution. On the other hand, the Local Group is thought to host at least as many ~150 galaxies [2] [3]. Indeed, the galaxy stellar mass function (GSMF) shows that dwarfs are the most abundant galaxies in the universe [4] [5] and yet detailed observations are comparatively (with more massive galaxies) sparse. Further underpinning their importance, it has been inferred that a great many of the Galaxy's present-day properties were determined in large part by its interactions in the past with galaxies around $z\sim2-3$ whose properties are similar to the dwarfs we see inhabiting the Local Group today.

For nearby galaxies, the distribution of individual stars in the $[\alpha/\mathrm{Fe}]-[\mathrm{Fe/H}]$ plane (hereafter $\alpha-$Fe plane) can tell us a great deal about their star formation histories. The observed relation between [α/Fe] and [Fe/H] in various stellar systems is affected by the timescales of production of the α-elements and Fe. The former are synthesised and released into the interstellar medium by core-collapse supernovae [6] whereas the latter result from both CCSNe *and* Type Ia supernovae [7] [8]. Since the two SNe types explode over markedly different timescales (CCSNe explode promptly following star formation, SNe Ia are delayed), these differences manifest

themselves in the overall slope of [α/Fe] as a function of [Fe/H].

According to models of galactic chemical evolution, because CCSNe alone contribute to the chemical enrichment of the ISM following the beginning of star formation in the nascent galaxy a totally flat sequence of high $[\alpha/Fe]$ at low $[Fe/H]$ forms. According to this theoretical formulation, when SNe Ia explosions begin to occur, the second order derivative of [α /Fe](t) goes up, and increasingly so as t approaches the e-folding timescale of the DTD. This results in the abundance ratio [α/Fe] decreasing as [Fe/H] increases [9]. The ensuing decrease in [α/Fe] would then form a characteristic turnover in the α-Fe plane commonly referred to as the "α knee".

It is reasonable to expect $[Fe/H]_{knee}$(the [Fe/H] at which the knee occurs) to scale with both the stellar mass and dynamical mass of a galaxy. In terms of the characteristic timescale of star formation, a short gas consumption timescale [1]could lead to the bulk of z=0 stellar mass being formed before SNe Ia are able to influence significantly the chemical evolution of the system \citep[see the analytical chemical evolution models of][for recent examples]andrews, weinberg-sudden-events. Particularly, this is believed to be the case in massive galaxies [10] [11] [12] [13] [14] [15]. While analytical models of chemical evolution and a number of observations demonstrate that a few of the Local Group Dwarfs (LGDs) and the Galactic thick disk show an α knee [16], a growing number of observations suggest that not all galaxies exhibit such a feature [17] [18] [19]. Doubt has also been cast on whether its formation corresponds to the onset of SNe Ia [11] [20].

Measurements of $[Fe/H]_{knee}$in dwarf galaxies show that the relationship between $M_\star$ and $[Fe/H]_{knee}$ is subject to a large degree of scatter at fixed $M_\star$ [21]. The generality of any conclusions may reasonably be called into question seeing as they are based on data for limited samples from a small number of galaxies. Clearly, an examination of this phenomenon using equivalent diagnostics on a statistically significant sample of galaxies formed in varying environments is required. However, observational databases are still not yet sufficiently large to afford such an approach.

In this paper we present an analysis of the Evolution and Assembly of GaLaxies and their Environments (EAGLE) simulations [22] [23] with the goal of characterising the α-Fe planes of a reasonably representative sample of simulated galaxies, to compare them to those observed in the Local Group. Cosmological hydrodynamical simulations provide an ideal laboratory to look at this problem, as instead of being limited to a single group of galaxies, we can examine the α-abundances of galaxies that formed in different environments, at different times and with different SFHs.

2. Data & methods

The EAGLE simulations are a suite of cosmological hydrodynamical simulations of the formation and evolution of galaxies in a ΛCDM cosmogony. A thorough description of these simulations can be found in [22], [23] and references therein. Our sample of galaxies originate from a simulation which followed the evolution of a periodic cube of side length $L = 34Mpc$ with an initial number of dark matter and gas particles numbering

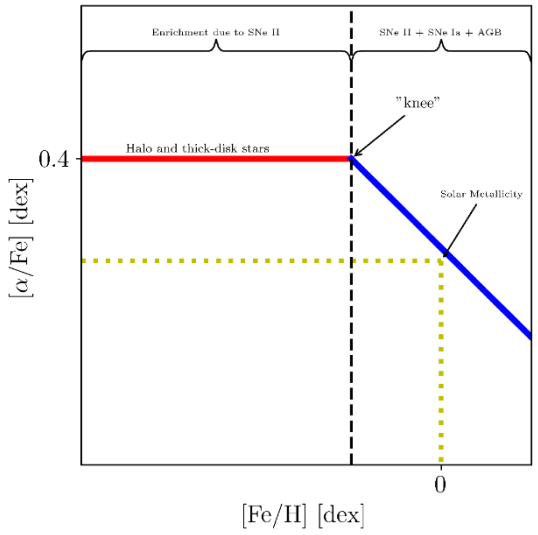

Figure 1. schematic alpha-Fe plane predicted by analytical GCE models

[1] The gas consumption timescale, t_g,is the inverse of what is termed the 'star formation efficiency'.

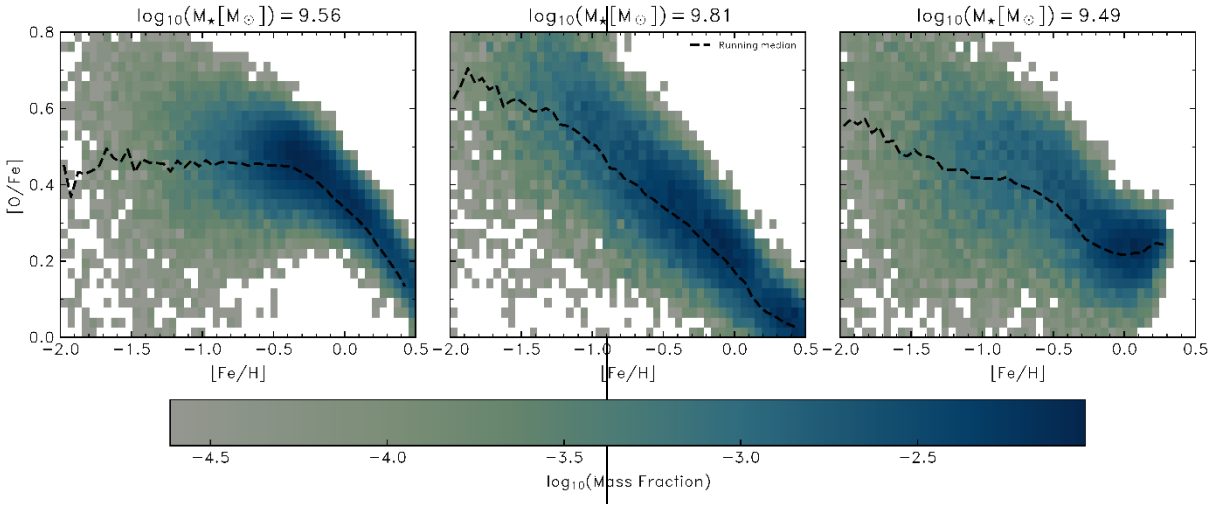

Figure 2. α-Fe planes of EAGLE galaxies showing i) classical knees, ii) single slopes and iii) inverted knees.

Gas particles which form stars in the EAGLE simulations behave as simples stellar populations forming with a Chabrier IMF [24] whose stars evolve and lose mass over time. The chemodynamics model uses the metallicity-dependent nucleosynthetic yields and lifetimes for massive stars, SNe Ia, CCSNe and the AGB phase [6] [25]. Additionally, EAGLE implements an exponential form of the SNe Ia DTD given by

$\dot{N}_{SNIa}(\tau) = \nu \frac{e^{-t/\tau}}{\tau}$,

where $\nu = 2 \times 10^{-3} M_{\odot}^{-1}$, the number of SNe Ia that explode per unit of initial mass and $\tau = 2Gyr$, the e-folding timescale of the DTD.

A cursory look at the α-Fe planes of the sample reveals that at $z = 0$ there is a great deal of diversity among the galaxy population in the simulation. Fig. 1 provides examples of what we consider to be the three typical categories of galaxies in the simulation. They are (from left-to-right) i) the classical knees, which resemble those in the Local Group, ii) the single slopes which have a single sequence of declining [α/Fe] and iii) the inverted knees, which exhibit a positively-sloped sequence of [α/Fe] at higher [Fe/H].

In order to characterize these distributions of stellar particles in a way consistent with methods used in the literature, we resort to parameterising the α-Fe plane as a piecewise linear function $f([Fe/H]_{knee}, [O/Fe]_{knee}, \theta_1, \theta_2)$, differing from [21] in that we place no restriction on the slopes of the plateau and shin components under the operating assumption that not all galaxies conform to the plateau-knee-shin morphology as we have seen from Fig. 2. We follow the procedure in [26], assuming there are no measurement uncertainties, to fit the model to the data using the Python package Pymc3 [27]. This is accomplished by maximising the log likelihood for the parameters of the model and using this optimal solution to initiate a Markov Chain Monte Carlo (MCMC) sampling of the posterior PDF of the parameters using the NUTS MCMC sampler [28]. Once the sampling is complete we take the median values of the posterior PDFs to be the 'true' values of each parameter and estimate their uncertainties by taking the interquartile ranges of the distributions. Fig. 3 gives an example of a fit to a classical knee.

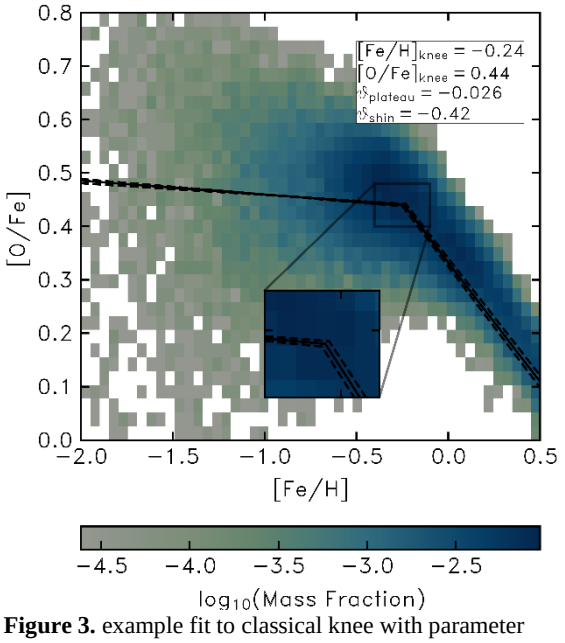

Figure 3. example fit to classical knee with parameter estimates illustrated.

With the model fits in hand, we select the classical knees as galaxies with

i. $\theta_{shin} + \sigma_{\theta_{shin}} < \theta_{plateau}$
ii. $\theta_{plateau} + \sigma_{\theta_{plateau}} < \theta_{shin}$
iii. $M_{\star,plateau}/M_{\star,total} > 0.25$
iv. $M_{\star,shin}/M_{\star,total} > 0.25,$

where θ refers to the slope of each respective component while σ denotes the uncertainty given by the interquartile range of the posterior PDF.

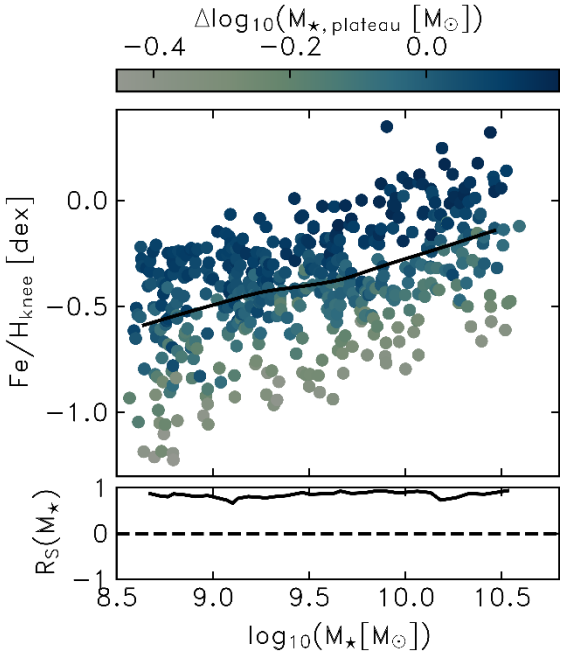

Figure 4. the MKR for EAGLE galaxies.

3. Results

Figs. 4 & 5 show some of the results of our paper. We find that the simulated galaxies show

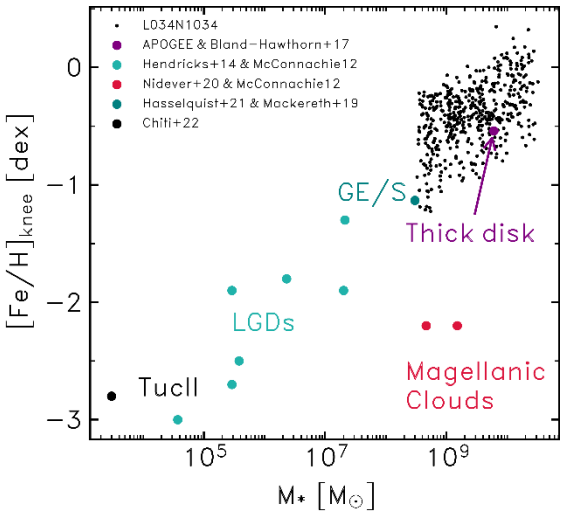

Figure 5. the MKR in L034N1034-RECAL compared to that measured thus far in the Local Group Dwarfs and Milky Way.

a relation between $[Fe/H]_{knee}$ and $M_{\star}$ (hereafter MKR) that is consistent within the errors with what has been measured by element abundance observations in the Local Group [16]. Furthermore, we find that the scatter in the MKR is driven largely by the amount of stellar mass that forms while the plateau is forming. We further explore the chemical evolution and star formation histories of the plateau and shin to explore this in our paper and find that the knee is not a consequence of merely the different timescales of CCSNe and SNe Ia enrichment, rather it is the result of a prolonged decline in the star formation rate (SFR) after a peak which causes a relative increase in the chemical enrichment by SNe Ia compared to CCSNe due to the shape of the SNe Ia DTD and the fact that the rate of CCSNe more promptly responds to changes in the SFR.

4. REFERENCES

[1] R. P. Schiavon, J. T. Mackereth, J. Pfeffer, R. A. Crain and J. Bovy, "The building blocks of the Milky Way halo using APOGEE and Gaia or Is the Galaxy a typical galaxy?," in *Star Clusters: From the Milky Way to the Early Universe*, 2020.

[2] Drlica-Wagner, A. et al., "Eight Ultra-faint Galaxy Candidates Discovered in Year Two of the Dark Energy Survey," *apj*, vol. 813, p. 109, November 2015.

[3] O. Newton, M. Cautun, A. Jenkins, C. S. Frenk and J. C. Helly, "The total satellite population of the Milky Way," *mnras*, vol. 479, pp. 2853-2870, September 2018.

[4] C. Li and S. D. M. White, "The distribution of stellar mass in the low-redshift Universe," *mnras*, vol. 398, pp. 2177-2187, October 2009.

[5] I. K. Baldry, S. P. Driver, J. Loveday, E. N. Taylor, L. S. Kelvin, J. Liske, P. Norberg, A. S. G. Robotham, S. Brough, A. M. Hopkins, S. P. Bamford, J. A. Peacock, J. Bland-Hawthorn, C. J. Conselice, S. M. Croom, D. H. Jones, H. R. Parkinson, C. C. Popescu, M. Prescott, R. G. Sharp and R. J. Tuffs, "Galaxy And Mass Assembly (GAMA): the galaxy stellar mass function at z < 0.06," *mnras*, vol. 421, pp. 621-634, March 2012.

[6] L. Portinari, C. Chiosi and A. Bressan, "Galactic chemical enrichment with new metallicity dependent stellar yields," *aap*, vol. 334, pp. 505-539, June 1998.

[7] S. E. Woosley and T. A. Weaver, "Sub–Chandrasekhar Mass Models for Type IA Supernovae," *apj*, vol. 423, p. 371, March 1994.

[8] K. Iwamoto, F. Brachwitz, K. C. H. I. Nomoto, N. Kishimoto, H. Umeda, W. R. Hix and F.-K. Thielemann, "Nucleosynthesis in Chandrasekhar Mass Models for Type IA Supernovae and Constraints on Progenitor Systems and Burning-Front Propagation," *apjs*, vol. 125, pp. 439-462, December 1999.

[9] F. Matteucci and E. Brocato, "Metallicity Distribution and Abundance Ratios in the Stars of the Galactic Bulge," *apj*, vol. 365, p. 539, December 1990.

[10] G. Worthey, S. M. Faber and J. J. Gonzalez, "MG and Fe Absorption Features in Elliptical Galaxies," *apj*, vol. 398, p. 69, October 1992.

[11] E. Tolstoy, V. Hill and M. Tosi, "Star-Formation Histories, Abundances, and Kinematics of Dwarf Galaxies in the Local Group," *araa*, vol. 47, pp. 371-425, September 2009.

[12] R. P. Schiavon, "Population Synthesis in the Blue. IV. Accurate Model Predictions for Lick Indices and UBV Colors in Single Stellar Populations," *apjs*, vol. 171, pp. 146-205, July 2007.

[13] J. Johansson, D. Thomas, J. Pforr, C. Maraston, R. C. Nichol, M. Smith, H. Lampeitl, A. Beifiori, R. R. Gupta and D. P.

Schneider, "SN Ia host galaxy properties from Sloan Digital Sky Survey-II spectroscopy," *mnras*, vol. 435, pp. 1680-1700, October 2013.

[14] C. Conroy, G. J. Graves and P. G. van Dokkum, "Early-type Galaxy Archeology: Ages, Abundance Ratios, and Effective Temperatures from Full-spectrum Fitting," *apj*, vol. 780, p. 33, January 2014.

[15] M. C. Segers, J. Schaye, R. G. Bower, R. A. Crain, M. Schaller and T. Theuns, "{The origin of the {\ensuremath{\alpha}}-enhancement of massive galaxies}," *mnras*, vol. 461, pp. L102-L106, September 2016.

[16] D. Horta, et al. "The chemical characterisation of halo substructure in the Milky Way based on APOGEE," *arXiv e-prints*, p. arXiv:2204.04233, April 2022.

[17] D. L. Nidever et al., "The Lazy Giants: APOGEE Abundances Reveal Low Star Formation Efficiencies in the Magellanic Clouds," *apj*, vol. 895, p. 88, June 2020.

[18] L. C. Vargas, M. C. Geha and E. J. Tollerud, "The Distribution of Alpha Elements in Andromeda Dwarf Galaxies," *apj*, vol. 790, p. 73, July 2014.

[19] L. C. Vargas, M. Geha, E. N. Kirby and J. D. Simon, "The Distribution of Alpha Elements in Ultra-faint Dwarf Galaxies," *apj*, vol. 767, p. 134, April 2013.

[20] D. Maoz and O. Graur, "{Star Formation, Supernovae, Iron, and {\ensuremath{\alpha}}: Consistent Cosmic and Galactic Histories}," *apj*, vol. 848, p. 25, October 2017.

[21] B. Hendricks, A. Koch, G. A. Lanfranchi, C. Boeche, M. Walker, C. I. Johnson, J. Peñarrubia and G. Gilmore, "The Metal-poor Knee in the Fornax Dwarf Spheroidal Galaxy," *apj*, vol. 785, p. 102, April 2014.

[22] J. Schaye, et al., "The EAGLE project: simulating the evolution and assembly of galaxies and their environments," *mnras*, vol. 446, pp. 521-554, January 2015.

[23] R. A. Crain, J. Schaye, R. G. Bower, M. Furlong, M. Schaller, T. Theuns, C. Dalla Vecchia, C. S. Frenk, I. G. McCarthy, J. C. Helly, A. Jenkins, Y. M. Rosas-Guevara, S. D. M. White and J. W. Trayford, "The EAGLE simulations of galaxy formation: calibration of subgrid physics and model variations," *mnras*, vol. 450, pp. 1937-1961, June 2015.

[24] G. Chabrier, "Galactic Stellar and Substellar Initial Mass Function," *pasp*, vol. 115, pp. 763-795, July 2003.

[25] P. Marigo, "Chemical yields from low- and intermediate-mass stars: Model predictions and basic observational constraints," *aap*, vol. 370, pp. 194-217, April 2001.

[26] D. W. Hogg, J. Bovy and D. Lang, "Data analysis recipes: Fitting a model to data," *arXiv e-prints*, p. arXiv:1008.4686, August 2010.

[27] J. Salvatier, T. V. Wiecki and C. Fonnesbeck, "Probabilistic programming in Python using PyMC3," *PeerJ Computer Science*, vol. 2, p. e55, 2016.

[28] M. D. Hoffman, A. Gelman and others, "The No-U-Turn sampler: adaptively setting path lengths in Hamiltonian Monte Carlo.," *J. Mach. Learn. Res.*, vol. 15, p. 1593–1623, 2014.

Sarah McDonald

Postgraduate Researcher

Astrophysics Research Institute

Red Supergiants in M31: The Humphreys-Davidson limit at high metallicity

Sarah McDonald[1], Ben Davies[1] **,** Emma Beasor[2]
[1]Astrophysics Research Institute, Liverpool John Moores University, Liverpool Science Park ic2,146 Brownlow Hill, Liverpool, L3 5RF, UK.
[2]NSF's National Optical-Infrared Astronomy Research Laboratory, 950 N. Cherry Ave., Tucson, AZ 85719, USA.
E-mail address: S.E.McDonald@2015.ljmu.ac.uk

Abstract. The empirical upper limit to Red Supergiant (RSG) luminosity, known as the Humphreys-Davidson (HD) limit, has been commonly explained as being caused by the stripping of stellar envelopes by metallicity-dependent, line-driven winds. As such, the theoretical expectation is that the HD limit should be higher at lower metallicity, where weaker mass-loss rates mean that higher initial masses are required for an envelope to be stripped. In this paper, we test this prediction by measuring the luminosity function of RSGs in M31 and comparing to those in the LMC and SMC. We find that $\log(L_{max}/L_\odot) = 5.53 \pm 0.03$ in M31 ($Z \gtrsim Z_\odot$), consistent with the limit found for both the LMC ($Z \sim 0.5\ Z_\odot$) and SMC ($Z \sim 0.25\ Z_\odot$), while the RSG luminosity distributions in these 3 galaxies are consistent to within 1σ. We therefore find no evidence for a metallicity dependence on both the HD limit and the RSG luminosity function and conclude that line-driven winds on the main sequence are not the cause of the HD limit.

Keywords. stars: massive – stars: evolution – supergiants

1. Introduction

It is well established that there is an empirical upper limit to Red Supergiant (RSG) luminosity [1,2], often referred to as the `Humphreys-Davidson (HD) Limit' [3]. The HD limit is often explained as being a manifestation of mass loss during the lifetime of the star, caused by strong stellar winds or episodic periods of mass-loss, where the fraction of mass lost from the stellar envelope is dependent on the initial mass of the star. Under this explanation, lower initial mass supergiants (~8M⊙-15M⊙) experience winds which are not strong enough to remove the entire hydrogen envelope on the main sequence (MS) [4,5], so the star is able to evolve to the RSG phase, where it resides before dying as a core-collapse supernova. Higher initial mass stars (~15M⊙-30M⊙) can lose a considerable fraction of their envelope, causing the star to undergo only a brief RSG phase before evolving to a Wolf Rayet (WR) star [6]. At even higher masses (≳30M⊙), the entire envelope can be lost by the time hydrogen in the core is exhausted, preventing evolution to the cool red side of the Hertzsprung-Russell (HR) diagram. These stars instead evolve directly from the MS to a WR star, completely bypassing the RSG phase [7]. Under this scenario, the HD limit therefore represents the luminosity which corresponds to the most massive star that may still experience a RSG phase. Evolutionary models predict that lower metallicity environments should produce more luminous supergiants due to this dependency of mass loss on metallicity [5,8]. This means the HD limit should therefore also be metallicity dependent.

The HD limit has been measured previously in the literature, the first being a hard upper limit of $\log(L/L_\odot) = 5.8 \pm 0.1$ in Humphreys & Davidson (1979) [3], using a sample of cool supergiants in the Milky Way and the Large Magellanic cloud (LMC) (later revised to $\log(L/L_\odot) = 5.66$ in Humphreys (1983) [9]. In Davies, Beasor & Crowther (2018) (hereafter, DCB18) [10], they revisit the HD limit in the Magellanic Clouds, with higher precision multi-wavelength photometry, finding an upper limit of

$\log(L/L_{\odot}) = 5.5$ for both the Small Magellanic Cloud (SMC) and the LMC, despite the metallicity of the SMC being roughly half that of the LMC. This is in tension with evolutionary theory.
In the present work, we complement the study of DCB18 with focus on the high luminosity end of the M31 RSG luminosity function as well as make quantitative comparisons with RSG populations in lower metallicity galaxies.

2. Method

2.1. Compiling the sample of RSGs

To locate our target stars, we constructed colour-magnitude diagrams (CMDs) using the Spitzer photometry [11], see Figure 1, and overplotted a sample of known RSGs from Massey & Evans (2016) [12] to define the location of RSGs in mid-IR colour-magnitude space. The total number of stars rejected from our sample are discussed further in Sections 2.1 and 3.3 in the full paper for this work [13], where reasons for rejection are outlined in detail. These stars were then cross-matched to Local Group Galaxy Survey (LGGS) UBVRI photometry [14], Gaia EDR3 photometry (BP and RP bands) and astrometry (proper motion and parallax) [15] and Two Micron All Sky Survey (2MASS) JHK photometry [16].

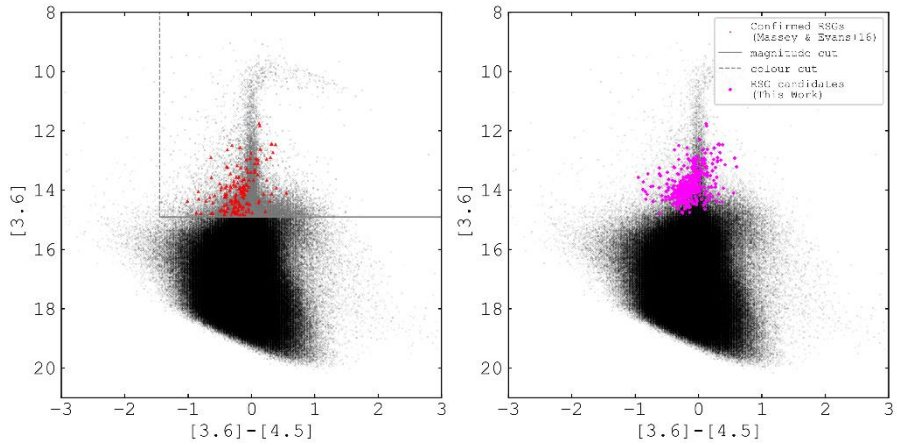

Figure 1:A colour magnitude diagram showing the selection process of detecting RSGs using mid-IR photometry from Spitzer [11]. The left panel (a) shows where colour and magnitude cuts were made around known RSGs in M31. The right panel (b) shows the RSG candidates detected (in magenta) which are used throughout this work.

2.2. Foreground Extinction

To correct for foreground extinction, we use an extinction map of M31 from [17], surveyed by The Panchromatic Hubble Andromeda Treasury project (PHAT) [18]. Each RSG candidate was then de-reddened according to the Cardelli (1989) [19] reddening law for the optical photometry, and the Rieke & Lebofsky (1985) [20] law for the near-IR.

3. Luminosity Distributions and L_{max}

3.1. Determining bolometric luminosity

We converted the de-reddened photometry into fluxes using Vega calibrated zero point fluxes for each filter from the SVO Filter Profile Service [21]. Using these fluxes, we plot spectral energy distributions (SEDs) for each RSG candidate and integrate under the SED to determine bolometric luminosity. Figure 2 shows the SEDs of the most luminous candidates.

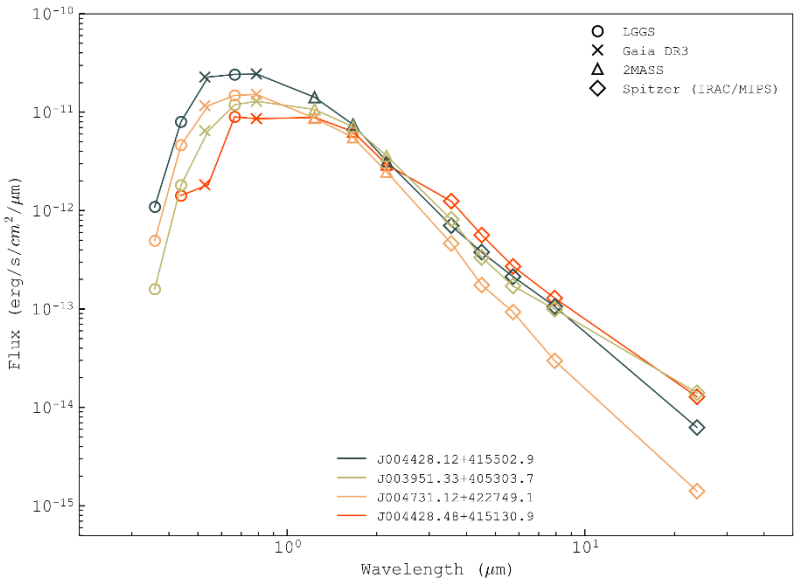

Figure 2: Spectral energy distributions (SEDs) of the most luminous Red Supergiant (RSG) candidates. These have log(L/L⊙) > 5.4 with complete de-reddened photometry ranging from the optical through to the mid-infrared. The symbols in the upper legend indicate the catalogue source of the photometry and the lower legend provides the LGGS star name for each candidate.

The observational luminosity function of M31 RSGs is seen in Figure 3. The light grey distribution shows the number of RSG candidates per log luminosity bin for M31. The two darker grey distributions show the number of RSG candidates we use in this study which are also found in previous M31 RSG studies. Each of these luminous RSGs are discussed in more detail in McDonald et. al. (2022) [13].

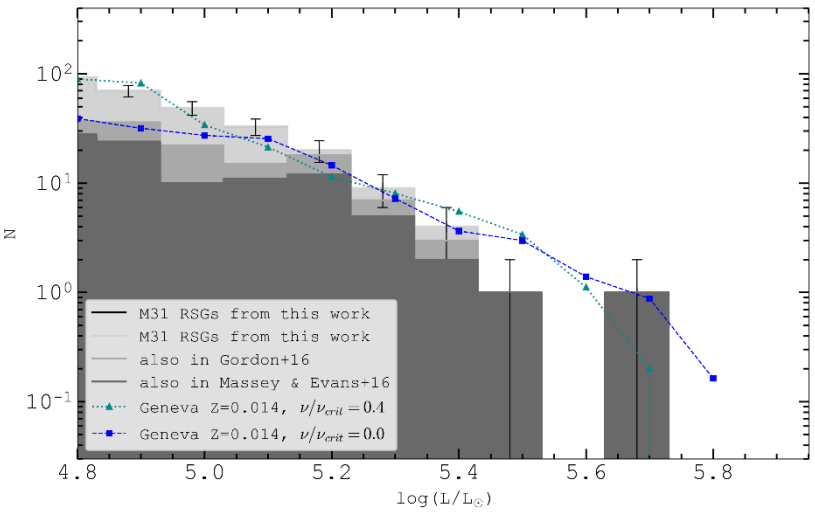

Figure 3: The Red Supergiant luminosity distribution for M31. The observed luminosity distribution from this work is shown in light grey, with the two darker grey distributions showing the number of RSG candidates we use in this study that are also found in previous M31 RSG studies. Over-plotted are the rotating (v/v_{crit} =0.4) and non-rotating (v/v_{crit} =0.0) model predicted distributions from the GENEVA models at solar metallicity (Z=0.014) [23].

4. Statistical Analysis

To make a broader test of the metallicity dependence of L_{max} and the luminosity function, we perform two comparisons. Firstly, we compare the empirical luminosity functions of the LMC and SMC with M31. Secondly, we compare the M31 luminosity function and L_{max} to theoretical expectations of lower metallicities using population synthesis.

4.1. Observational comparisons between the LMC and SMC

We look at the cumulative RSG luminosity function for M31 and compare with the empirical SMC and LMC distributions from DCB18, looking at all RSGs with $\log(L/L_{\odot}) > 5$, where our sample is considered to be complete. The left panel (a) of Figure 4 shows the similarities of the observed cumulative luminosity functions for M31, SMC and LMC. We perform a Kolmogorov-Smirnov (KS) test to evaluate these similarities by measuring the differences between the cumulative distribution functions. We find for the empirical M31 distribution compared with the SMC and LMC, a 60% and 44% probability, respectively, that they are drawn from the same parent distribution. Hence, the probability that the RSG luminosity function in the three galaxies are consistent with one another is within 1σ. Furthermore, each galaxy has the same L_{max} to within 0.1dex, at $\log(L/L_{\odot}) \sim 5.5$.

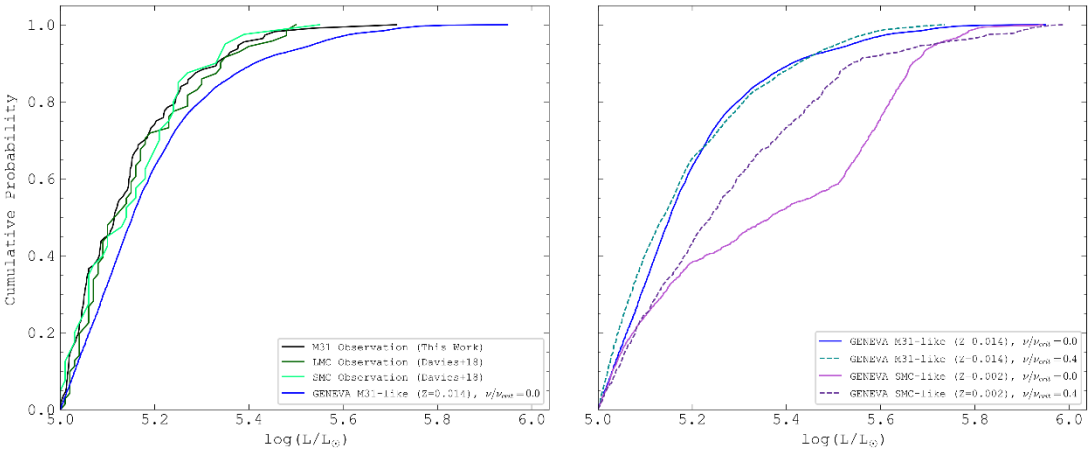

Figure 4:Left Panel (a): The cumulative luminosity distribution of all the M31 RSGs with an observational luminosity $\log(L/L_{\odot}) > 5$ from this work, as well as for the Large and Small Magellanic Clouds from DCB18 [10]. Right panel (b): Same as (a) but instead using the model luminosity function predicted by GENEVA at both solar and SMC-like metallicities [23,22] for both the rotating and non-rotating models.

We do the same for the model cumulative luminosity function of RSGs at SMC-like (Z=0.002) metallicity (SMC-like tracks are from Georgy et. al. (2013) [22]) when compared with M31, seen in the right panel (b) of Figure 4. Here we find a probability of 5% (rotating) and 0.1% (non-rotating) for the M31 models compared with observations and a 0.02% (rotating) and $\sim 10^{-6}$% (non-rotating) probability for the SMC models compared with observations. These low probabilities lead us to conclude that there is little similarity between the model distributions in the two galaxies and they are unlikely to be drawn from the same parent distribution.

4.2 Comparisons to theoretical predictions of Lmax

To investigate the effects of sample size on L_{max}, we perform another Monte Carlo experiment to find the average L_{max} for each sample size of N cool supergiants with $\log(L/L_{\odot}) > 5$. The results of this Monte Carlo are shown in Figure 5 where the empirical L_{max} for the sample size we observe for that galaxy is denoted by the black star. Although M31 shows agreement within 3σ, the SMC shows a disagreement beyond the 99.7% confidence limit.

In summary, we find no significant difference in L_{max} within the errors across a metallicity baseline of ($0.25Z_{\odot}$ to $\gtrsim Z_{\odot}$). This is in clear disagreement with theoretical expectations because L_{max} predictions from the models are simply too high compared to observational measurements and this effect is predicted to only increase with decreasing metallicity.

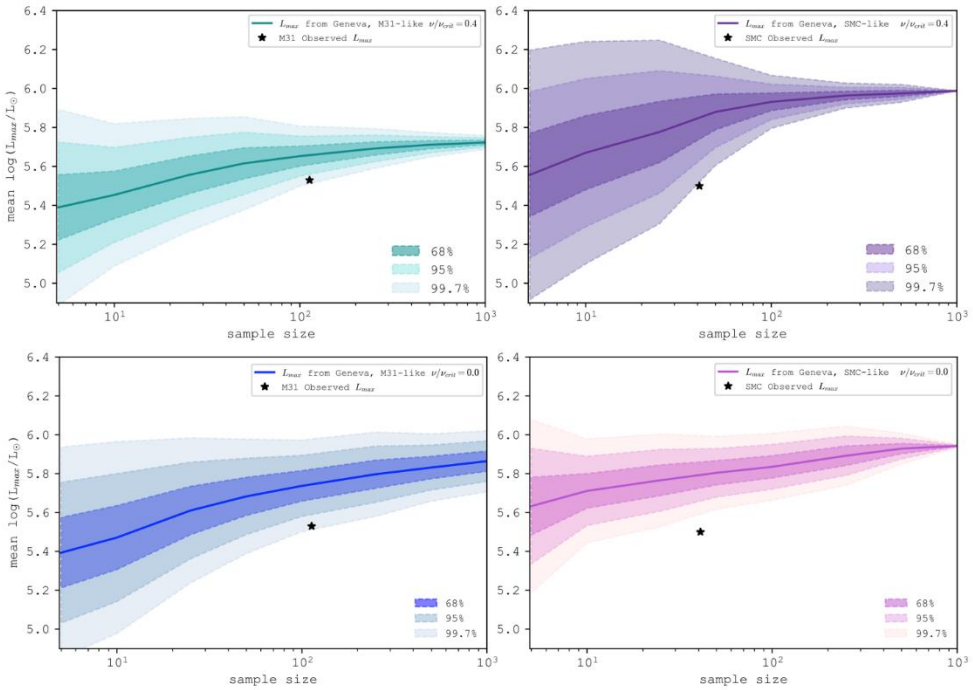

Figure 5: The expected L_{max} for a range of sample sizes as predicted by the GENEVA rotating models for both solar (Z=0.014) and SMC-like (Z=0.002) metallicities. The shaded regions indicate the confidence limits on L_{max} as shown in the legend and the black stars indicate the observed L_{max} and sample size for M31 from this work and the same for the SMC from DCB18.

5. Summary & Conclusions

We compiled a sample of mid-IR selected cool supergiants to measure the luminosity function of the red supergiant (RSG) population in M31 to investigate the Humphreys-Davidson limit (L_{max}).

- We find that the luminosity function of RSGs is independent of metallicity, based on the range of metallicities studied here (from SMC-like to M31-like).

- L_{max} is also independent of metallicity, where we find the HD limit for M31 is $\log(L_{max}/L_{\odot})$ $\log(L_{max}/L_{\odot}) = 5.53 \pm 0.03$ within 0.1dex of the SMC and LMC. We are in agreement with DCB18 who find a lack of evidence for a metallicity dependent L_{max}. This suggests that mass loss from line-driven winds are ***not*** the cause of the HD limit.

- A population synthesis analysis shows that the single star Geneva evolutionary models not only over-predict the number of luminous cool supergiants at the high luminosity end, but also over-predict L_{max} particularly at lower metallicities.

6. Future work

This work was followed up by a study of the sample of RSGs found through our mid-IR cuts, where we calculate the mass loss rates of these stars. This was achieved by modelling the dust shells of the stars using the radiative transfer code DUSTY (McDonald in prep. (2023)). In the future, spectroscopic follow up of these stars would be beneficial, since we found ~170 RSG candidates not yet found/confirmed in previous work in the literature. Further, we have began the first steps to use machine learning techniques to predict the mass loss rates of RSGs based on fluxes from their SEDs and hope to apply this model to RSGs from other galaxies such as M33.

References:

[1] Stothers, R. 1969, ApJ, **155, 935**
[2] Sandage, A., & Tammann, G. A. 1974, ApJ, **191, 603**
[3] Humphreys, R. M., & Davidson, K. 1979, ApJ, **232, 409**
[4] Maeder, A. 1981, A&A, **102, 401**
[5] Maeder, A., & Meynet, G. 2003, in IAU Symposium, Vol. 212, A Massive Star Odyssey: From Main Sequence to Supernova, ed. K. van der Hucht, A. Herrero, & C. Esteban, **267**
[6] Stothers, R., & Chin, C. W. 1979, ApJ, **233, 267**
[7] Stothers, R., & Chin, C. W. 1978, ApJ, **226, 231**
[8] Kudritzki, R. P., Pauldrach, A., & Puls, J. 1987, A&A, **173, 293**
[9] Humphreys, R. M. 1983, ApJ, **265, 176**
[10] Davies, Crowther & Beasor. 2018, MNRAS, **478, 3138**
[11] Khan, R. 2017, ApJS, **228, 5**
[12] Massey, P., & Evans, K. A. 2016, ApJ, 826, 224
[13] McDonald, S. L. E., Davies, B., & Beasor, E. R. 2022, MNRAS, 510, 3132
[14] Massey, P., Olsen, K. A., Hodge, P. W., Jacoby, G. H., McNeill, R. T., Smith, R. C., & Strong, S. B. 2006, in American Astronomical Society Meeting Abstracts, **Vol. 209**, American Astronomical Society Meeting Abstracts, **27.01**
[15] Gaia Collaboration. 2020, VizieR Online Data Catalog, **I/350**
[16] Cutri, R. M., et al. 2003, VizieR Online Data Catalog, **II/246**
[17] Dalcanton, J. J., et al. 2015, ApJ, **814, 3**
[18] Dalcanton, J. J., et al. 2012, ApJS, **200, 18**
[19] Cardelli, J. A., Clayton, G. C., & Mathis, J. S. 1989, ApJ, **345, 245**
[20] Rieke, G. H., & Lebofsky, M. J. 1985, ApJ, **288, 618**
[21] Rodrigo, C., & Solano, E. 2020, in Contributions to the XIV.0 Scientific Meeting (virtual) of the Spanish Astronomical Society, **182**
[22]Georgy,C., et al. 2013, A&A, **558, A103**
[23] Ekstrom, S., et al. 2012 A&A, **537, A146**

Kyle Medler

Postgraduate Researcher

Astrophysics Research Institute

Flat-topped NIR profiles originating from an unmixed helium shell in the Type IIb SN 2020acat

K. Medler[1], P.A. Mazzali[1,2], C. Ashall[3], J. Teffs[4], M. Shahbandeh[5], B. Shappee[6]
[1] Astrophysical Research Institute, Liverpool John Moores University, Liverpool L3 5RF, UK
[2] Max-Planck Institute for Astrophysics, Karl-Schwarzschild-Str. 1, D-85748 Garching, Germany
[3] Department of Physics, Virginia Tech, Blacksburg, VA 24061, USA
[4] Aretè Associates, 3194 N Swan Rd, Tucson, AZ 85712
[5] Department of Physics, Florida State University, 77 Chieftan Way, Tallahassee, FL 32306, USA
[6] Institute for Astronomy, University of Hawai'i at Manoa, 2680 Woodlawn Dr., Hawai'i, HI 96822, USA
Email: K.Medler@2019.ljmu.ac.uk

Abstract:
The Near Infrared (NIR) spectra of the Type IIb supernova (SN IIb) SN 2020acat, obtained at various times throughout the optical follow-up campaign, are presented here. The dominant He_I 1.0830 μm and 2.0581 μm features are seen to develop flat-topped P-Cygni profiles as the NIR spectra evolve towards the nebular phase. The nature of the NIR helium peaks imply that there was a lack of mixing between the helium shell and the heavier inner ejecta in SN 2020acat. Analysis of the flat-top features showed that the boundary of the lower velocity of the helium shell was ~ 3 - 4 $x10^3$ kms^{-1}. The NIR spectra of SN 2020acat were compared to both SN 2008ax and SN 2011dh to determine the uniqueness of the flat-topped helium features. While SN 2011dh lacked a flat-topped NIR helium profile, SN 2008ax displayed NIR helium features that were very similar to those seen in SN 2020acat, suggesting that the flat-topped feature is not unique to SN 2020acat and may be the product of the progenitors structure.

Keywords: Supernovae:General-Supernovae:SN 2020acat

1. Introduction

Core-collapse supernovae (CC-SNe) result from high mass ($M > 8M_\odot$) stars that undergo rapid gravitational collapse. The structure of the stars outer hydrogen and helium envelops strongly influences the SNe observational properties, creating several different types of CC-SNe [1]. One subcategory is the stripped envelope supernovae (SE-SNe), which are characterised by similar light curve shapes, and spectra that display either weak or no hydrogen features [2,3]. The presence of hydrogen within the outer envelope of SE-SN progenitors, with a hydrogen mass range of $M_H = 0.033 – 1\ M_\odot$ [4,5], results in a type IIb SN (SN IIb).

The NIR spectra provide vital information on the structure of the SN progenitor, especially the helium envelope. The Near-Infrared (NIR) spectra of SNe IIb are dominated by strong hydrogen and helium lines [6,7]. Although the H_I *Pa* lines lie in a region heavily influenced by telluric effects, increasing the difficulty in obtaining clear observations. Despite this problem, both hydrogen and helium lines are expected to display P-Cygni profiles under the assumption of spherically expanding ejecta.

Here we present the NIR spectra of SN 2020acat. In Section 2, we provide an overview on SN 2020acat and the results obtained from analysis of the photometry and optical spectra. In Section 3, we analyse the structure of the NIR helium features seen in SN 2020acat. Then in Section 4, we look at other SNe IIb NIR spectra to determine how unique the flat-topped helium structure is. Finally in Section 5, we present the conclusions from analysis of the NIR spectra of SN 2020acat and other SNe IIb.

2. SN 2020acat

SN 2020acat was a rapidly rising SN IIb caught within ~1 day of explosion on December 9th 2020 (MJD_{exp} = 59192.01) at a redshift of z = 0.0079 [8]. Photometric analysis showed that SN 2020acat had a very fast rise time for a SNe IIb, reaching a bolometric peak of $L_{peak} = 3.09^{+1.28}_{-0.90}$ $x10^{42}$ $ergs^{-1}$ in 14.6 ± 0.3 days, approximately 4 - 5 days faster than typical SNe IIb. [8] estimated that SN 2020acat had a ^{56}Ni mass of $M_{Ni} = 0.13 \pm 0.02\ M_\odot$, along with an ejecta mass of $M_{ejc} = 2.3 \pm 0.3\ M_\odot$, and a kinetic energy of $E_k = 1.2 \pm 0.2$ $x10^{51}$ erg. While the ejecta mass is average for SNe IIb, both M_{Ni} and E_k of SN 2020acat are slightly larger [9,10].

Table 1: Observational details for the NIR spectra of SN 2020acat. Phase is given from explosion date (MJD_{exp} = 59192.01) and given in rest frame. Air mass is the average air mass over the observation period.

UT date	MJD	Phase [days]	Telluric STD	Air Mass	Exposure
24-12-2020	59207.66	15.53	HIP54815	1.16	1200
23-02-2021	59268.33	75.72	HIP54815	2.54	1200
22-04-2021	59326.33	133.27	HD asdf	1.16	1200
24-05-2021	59358.34	165.02	HD asdf	1.37	1200

The optical spectra of SN 2020acat initially displayed prominent hydrogen and helium lines, with a strong H_α signature lasting for ~100 days. In the nebular phase, oxygen emission dominates over calcium. Finally, from analysis of photometry and spectra it was suggested that SN 2020acat originated from a compact progenitor with an initial mass of M_{ZAMS} between 15-20 $M_\odot$ [8].

3. He_I 1.0830 µm and 2.0581 µm Features

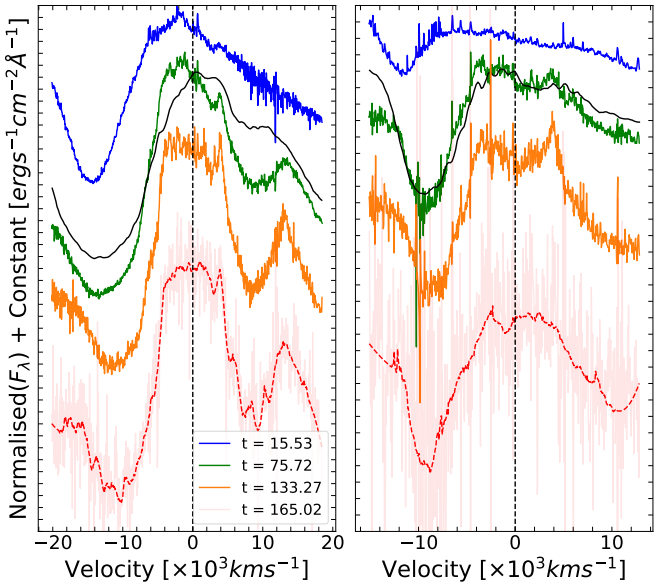

Figure 1: Velocity evolution of the He_I 1.0830 µm and 2.0581 µm lines. Model fit to the day 75 spectrum (solid black line) shows a good fits the He_I .0581 µm feature. The flat-top feature of the He_I 1.0830 µm line develops the day 75 and 133 spectra, while the He_I 2.0581 µm line develops earlier between the day 15 and 75 spectra.

The evolution of the helium lines, shown in Figure 1, display the most drastic evolution. The evolution of the He_I 1.0830 µm and 2.0581 µm line velocity given in Table 2. In the earliest spectrum both helium features display broad P-Cygni profiles, as expected from spherically symmetric ejecta expanding at high velocity. The He_I 1.0830 µm line displayed a faster overall velocity, falling from 14.4 to 10.7 $x10^3$ kms^{-1}, compared to the He_I 2.0581 µm line, which declined from 11.7 to 8.6 $x10^3$ kms^{-1}. The He_I 2.0581 µm line velocity declines rapidly between days 15.53 and 75.72, roughly twice the decline seen in the He_I 1.0830 µm line velocity during this period. This is likely due to the weakness of the He_I 2.0581 µm compared to the He_I 1.0830 µm line. After the initial rapid decline the two line velocities continue to evolve at a similar pace.

Table 2: Line velocity of the He_I 1.0830 µm and 2.0581 µm lines derived from fitting the absorption minimum with a Gaussian fit. Associated errors obtained from fitting errors and noise within the spectra.

Phase	He_I 1.0830 µm velocity[$x10^3$ kms^{-1}]	He_I 2.0581 µm velocity[$x10^3$ kms^{-1}]
15.53	14.4 ± 0.4	11.7 ± 0.5
75.72	13.3 ± 0.9	9.3 ± 1.0
133.27	11.4 ± 0.9	8.7 ± 0.9
165.02	10.7 ± 0.9	8.6 ± 3.6

As the spectrum evolves the peaks of the He_I lines shift closer to their rest wavelengths and become flatter in shape. This is first seen clearly in the day 133.27 spectrum, where the features appear flat-topped with distinct cutoffs on either side of the lines' rest wavelength, and is still visible in the day 165.02 spectrum. The presence of a small peak just red of both He_I lines is also interesting. We originally interpreted the feature red of the He_I 1.0830 µm peak as resulting from the Pa_γ λ 1.094 µm line. However, a small peak is also seen near He_I 2.0581 µm, at a similar displacement from the emission line, in a region with no associated hydrogen or heavy element emission lines. This strongly suggests that the small peaks are not due to different emission lines, and instead mark the start of the helium emission shell, placing a strong constraint on the lower limit of the helium shell velocity.

The day 75 spectrum was fit with a synthetic spectrum obtained using a modified version of the model described in [11], where helium was removed below a velocity of 5000 kms^{-1}. The synthetic spectrum was computed using our Montecarlo SN spectrum synthesis code [12-14], including a non-thermal module for He_I [4]. The synthetic spectrum reproduced both the flat-topped P-Cygni profile of the NIR Helium features, shown in Figure 1, and the standard P-Cygni profile observed in the optical spectra shown in [8] at earlier times. While the synthetic spectrum reproduces the

small red peak seen in both Helium lines, a feature expected as a result of a sharp inner cut-off of the helium shell, it fails to reproduce the HeI 1.0830 μm feature in detail. This is likely caused by the contribution of other lines in this region (C_I, Si_{II}).

Table 3: v_{edg} obtained from fitting the flat-topped He_I 1.0830 μm and 2.0581 μm emission peaks.

Phase	1.0830 μm v_{edg} [x10^3 kms^{-1}]	2.0581 μm v_{edg} [x10^3 kms^{-1}]
75.72	4.0 ± 0.5	3.9 ± 0.5
133.27	3.7 ± 0.5	3.9 ± 0.5
165.02	3.6 ± 1.0	3.6 ± 1.0

The widths of the flat-topped peaks were determined by fitting a Super-Gaussian function to the He_I 1.0830 μm and 2.0581 μm peaks. The fit allows for the edges of the flat-top to be determined, while also fitting to the shape of the emission profile outside this region. It was assumed that the peaks are symmetrical around the rest wavelength once the flat-topped shape emerged. The edge velocities, v_{edg}, of the helium lines are given in Table 3. As SN 2020acat evolves, the width of the flat-top decreases as ejecta expand and the density of the emitting helium shell appears to decrease slightly, although this is within the measurement errors. The existence of a minimum helium velocity indicates that the helium shell was not mixed down into the inner ejecta. To investigate the possibility of a non-mixed helium shell, we compared the velocity of the $[O_I]$ 6300, 6363 feature with the width of the flat-topped He_I 1.0830 μm and 2.0581 μm features. At both epochs the Full-Width Half-Maximum (FWHM) of the $[O_I]$ emission peak coincides with the v_{edg} of the helium shell to within ~100 kms^{-1} (see Figure 2). The lack of overlap between the helium and oxygen velocities strongly implies that the bulk of the two shells were not mixed prior to explosion.

4. SNe IIb Helium Structure

The flat-topped He_I 1.0830 μm and 2.0581 μm features seen in the late time spectra of SN 2020acat imply a cut off to the helium shell at low velocity. The question arises whether this feature is unique to SN 2020acat or if it was seen in other SNe IIb. At early times (t < 60 days), when the majority of NIR observations are obtained [7], SN 2020acat does not clearly show flat-topped helium features as the photosphere had not yet receded deep enough into the inner ejecta.

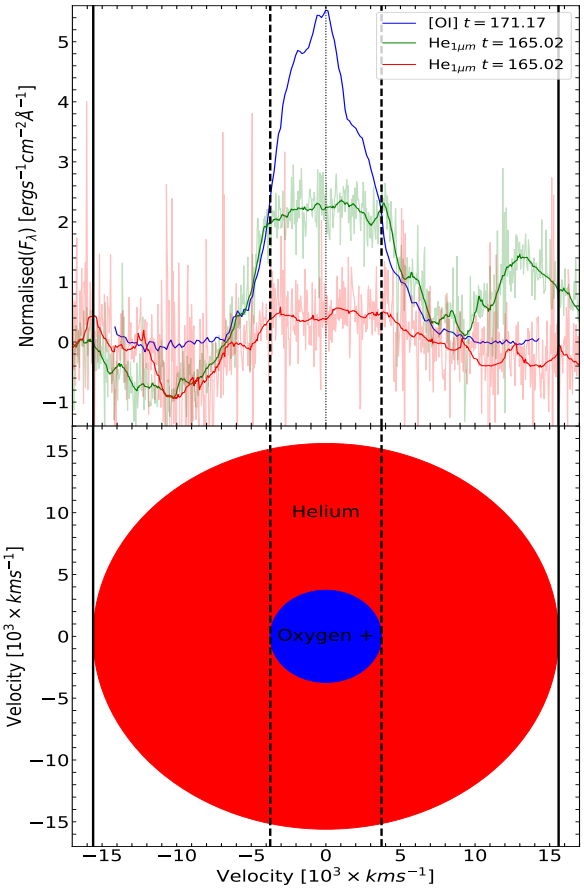

Figure 2: Top: Comparison of the late time $[O_I]$ 6300, 6363 peak and the smoothed NIR He_I features. All features have been scaled to the continuum. The solid, dashed and dotted vertical lines correspond to the Helium shell v_{edg}, the FWHM of the $[O_I]$ feature and the emission wavelength of each feature respectively. Bottom: Structure of the helium and oxygen rich shells in SN 2020acat corresponding to the velocities derived from the spectra.

As such, only SN 2008ax [15] and SN 2011dh [16] possess observations, with high enough S/N, to allow for good comparisons with SN 2020acat. The late-time He_I 1.0830 μm and 2.0581 μm features of SN 2020acat are compared with those of SN 2008ax and SN 2011dh, obtained 11-06-2008 and 16-12-2011 respectively, in Figure 3. It should be noted that the NIR spectrum of SN 2011dh does not extend to the He_I 2.0581 μm line, so only SNe 2008ax and 2020acat are displayed in Figure 3 (right panel).

SN 2008ax also displays narrow flat-topped NIR helium profiles, while SN 2011dh displays only a strong emission profile. When compared to SN 2020acat, the HeI 1.0830 μm feature of SN 2008ax exhibits a more prominent slope along the top of the feature peaking at the blue edge of the flat-top. On the other hand, the He_I 2.0581 μm line shows more of a symmetric double peak centred on the emission line, similar in nature to the line seen in the day 133.27 spectrum of SN 2020acat,

although significantly narrower. It was suggested that the shape of the He_I 1.0830 μm and 2.0581 μm lines in SN 2008ax result from a non-uniform distribution of ^{56}Ni within the ejecta [15]. However, [17] suggested that the cause of flat-top shape seen in SN 2008ax was instead the result of a torus-shaped distribution of helium, along with an additional asymmetry along the line of sight to induce the strong blue peak seen in the He_I 1.0830 μm line. Their models confined the majority of heavy elements to within the core with some mixing between the inner elements and the bottom of the helium shell.

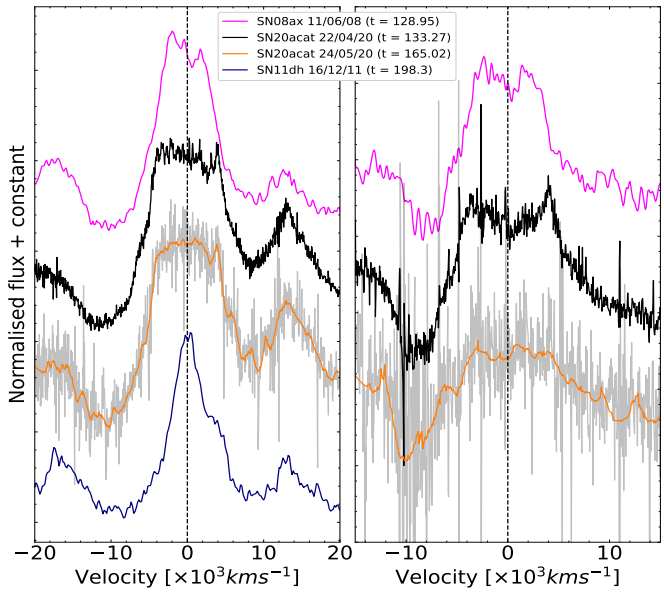

Figure 3: Comparison of the HeI 1.0830 μm (left) and the HeI 2.0581 μm (right) feature within the late time spectra of SN 2008ax (magenta), SN 2011dh (blue) and SN 2020acat (black and orange).

The question remains what could cause the helium features to display flat-topped shapes in SNe 2008ax and 2020acat, but not in SN 2011dh. The flat-topped profiles may be explained by stellar evolution, where the He shell does not mix with the inner regions which have a much higher molecular weight. However, there are several possibilities that could give rise to flat-topped profiles, including asphericity in the explosion which could lead to element mixing in velocity space [18]. The observed line profiles would then depend on the orientation of the line of sight. The small number of SNe IIb with late time NIR spectra, however, means that this suggestion is speculative in nature and requires a more extensive data set to determine its validity.

5. Conclusions

SN 2020acat displays interesting NIR spectra, which are dominated by the NIR helium lines and at later times display strong oxygen and magnesium lines. The He_I features display a curious evolution, transitioning from a standard P-Cygni profile during the photospheric phase into a more flat-topped shape at late times. From the width of the two flat-topped peaks a lower limit on the velocity of the helium shell was obtained. Fitting the flat-top features revealed a minimum velocity of the helium shell of around ~4.0 ± 0.5 x10^3 kms^{-1}, which seem to slightly decline to a final velocity of ~3.6 ± 1.0 x10^3 kms^{-1} roughly 90 days later. The shape of these features are thought to originate from a lack of emitting helium within the ejecta material brought about by a low optical depth within the central region of the ejecta. Through a comparison with the [O_I] 6300, 6363 emission peak it was found that there is a lack of overlap between the helium and oxygen features, strongly suggesting that there is little or no mixing between the helium and oxygen-rich shells.

A comparison with other SNe IIb NIR spectra was done to determine if the flat-top features were unique to SN 2020acat. While SN 2008ax displayed a similar feature, although significantly smaller in width, SN 2011dh displayed a sharp emission profile expected for spherically symmetric ejecta. A non-spherically shaped helium shell is likely to be the origin for the flat-topped profile seen in SN 2008ax and SN 2020acat, which may be linked to the structure of their progenitors. If the feature is indeed linked to the nature of the SNe progenitor, it may be used to determine the structure of the progenitor of events with limited observations. However, due to the limited number of SE-SNe NIR spectra, a larger sample of NIR spectra is currently needed to confirm the connection between progenitor structure and shape of the NIR helium feature.

6. References

[1] Matheson T., Filippenko A. V., Li W., Leonard D. C., Shields J. C., 2001, AJ, 121, 1648
[2] Clocchiatti A. & Wheeler J. C., 1997, ApJ, 491, 375
[3] Filippenko A. V., 1997, ARA&A, 35, 309
[4] Hachinger S., Mazzali P. A., Taubenberger S., Hillebrandt W., Nomoto K., Sauer D. N., 2012, MNRAS, 422, 70
[5] Gilkis A. & Arcavi I., 2022, MNRAS, 511, 691
[6] Martin W. C., 1987, Phys. Rev. A, 36, 3575
[7] Shahbandeh M., et al., 2022, ApJ, 925, 175
[8] Medler K., et al., 2022, MNRAS, 513, 5540
[9] Lyman J. D., Bersier D., James P. A., Mazzali P. A., Eldridge J. J., Fraser M., Pian E., 2016, MNRAS, 457, 328
[10] Prentice S. J., et al., 2019, MNRAS, 485, 1559
[11] Teffs J., Ertl T., Mazzali P., Hachinger S., Janka T., 2020, MNRAS, 492, 4369
[12] Mazzali P. A. & Lucy L. B., 1993, A&A, 279, 447
[13] Lucy L. B., 1999, A&A, 344, 282
[14] Mazzali P. A., 2000, A&A, 363, 705
[15] Taubenberger S., et al., 2011, MNRAS, 413, 2140
[16] Ergon M., et al., 2015, A&A, 580, A142
[17] Maurer I., Mazzali P. A., Taubenberger S., Hachinger S., 2010, MNRAS, 409, 1441
[18] Mazzali P. A., et al., 2005, Science, 308, 1284

Stephen Molyneux

Postgraduate Researcher

Astrophysics Research Institute

Spectroscopic confirmation of a gravitationally lensed Lyman-break galaxy at $z_{[C\,II]}$= 6.827 using NOEMA

SJ Molyneux[1,2], R Smit[1], D Schaerer[3,4], RJ Bouwens[5], L Bradley[6], JA Hodge[5], SN Longmore[1], S Schouws[5], P van der Werf[5], A Zitrin[7], S Phillips[1]

[1]Astrophysics Research Institute, Liverpool John Moores University, 146 Brownlow Hill, Liverpool L3 5RF, UK
[2]European Southern Observatory, Karl-Schwarzschild-Strasse 2, D-85748 Garching, Germany
[3]Observatoire de Geneve, `Universite´ de Genève, 51 Ch. des Mail-lettes, CH-1290 Versoix, Switzerland
[4]CNRS, IRAP, 14 avenue E. Belin, F-31400 Toulouse, France
[5]Leiden Observatory, Leiden University, NL-2300 RA Leiden, the Netherlands
[6]Space Telescope Science Institute, Baltimore, MD 21218, USA
[7]Physics Department, Ben-Gurion University of the Negev, PO Box 653, Be'er-Sheva 8410501, Israel
E-mail address: s.j.molyneux@2019.ljmu.ac.uk

Abstract. We present the spectroscopic confirmation of the brightest known gravitationally lensed Lyman-break galaxy in the Epoch of Reionization (EoR), A1703-zD1, through the detection of [C II] 158μm at a redshift of z = 6.8269 ± 0.0004. This source was selected behind the strong lensing cluster Abell 1703, with an intrinsic luminosity and a very blue *Spitzer*/Infrared Array Camera (IRAC) [3.6] – [4.5] colour, implying high equivalent width line emission of [O III] + Hβ. [CII] is reliably detected at 6.1σ co-spatial with the rest-frame ultraviolet (UV) counterpart, showing similar spatial extent. Correcting for the lensing magnification, the [C II] luminosity in A1703-zD1 is broadly consistent with the local $L_{[CII]}$ – star formation rate (SFR) relation. We find a clear velocity gradient of 103 ± 22 km s^{-1} across the source that possibly indicates rotation or an ongoing merger. This is the first time that the Northern Extended Millimeter Array (NOEMA) has been successfully used to observe [C II] in a 'normal' star-forming galaxy at z > 6, and our results demonstrate its capability to complement the Atacama Large Millimeter/submillimeter Array (ALMA) in confirming galaxies in the EoR.

Keywords. galaxies: evolution – galaxies: formation – galaxies: high-redshift

1 INTRODUCTION

In the past decade hundreds of galaxies have been identified in the Epoch of Reionization (EoR), selected from their rest-frame ultraviolet (UV) light, using Hubble Space Telescope (HST) and ground-based optical/near-infrared observatories (see Stark 2016, for a review and references therein). However, only a fraction of these sources have spectroscopic redshift determinations and we have a limited understanding of their physical properties. One reason for this is the difficulty in obtaining Lyman α (Lyα) observations at such high redshifts, due to its absorption by neutral hydrogen in the intergalactic and interstellar medium (IGM and ISM; with detected Lyα emitters possibly residing in early ionized bubbles; e.g. Jung et al. 2020; Endsley et al. 2021).

In recent years the Atacama Large Millimeter/submillimeter Array (ALMA) has transformed this field by confirming redshifts of galaxies out to z = 9 (e.g. Hodge & da Cunha 2020; Bouwens et al. 2021) and providing the first view of their dust obscured star formation (e.g. Laporte et al. 2017; Bowler et al. 2018; Schouws et al. 2021), the kinematics of these sources (e.g. Fujimoto et al. 2019; Hashimoto et al. 2019; Ginolfi et al. 2020), the cool gas traced by [C II], and highly ionized gas traced by [O III] (e.g. Laporte et al. 2017; Harikane et al. 2019; Hashimoto et al. 2019). Uncovering the physical

properties of these primordial systems is fundamental to understanding the evolution of the first generation of galaxies and their role in cosmic reionization.

Recently, the Plateau de Bure Interferometer (PdBI) has been upgraded to the Northern Extended Millimeter Array (NOEMA). The upgrades have increased the number of antennae from six to 10 (with two more planned to eventually increase the total number to 12) providing more collecting power and therefore increased sensitivity to observe these fainter sources. A new correlator has also been installed, which can cover a larger frequency range in one set-up, enabling faster line scans. These upgrades arguably make NOEMA the most powerful interferometer in the Northern hemisphere, and therefore might play an important role in observing [C II] in galaxies at $z > 6$.

Here we report on a line search for [C II] 158μm with NOEMA, targeting three galaxies in the Northern hemisphere at $z \sim 6.6 – 6.9$. The targets were selected from a sample of Lyman-break galaxies, with high-precision photometric redshifts (Smit et al. 2014, 2015). A1703-zD1 is the standout target, lying behind the strong lensing cluster Abell 1703, with a magnification of ∼9 (Bradley et al. 2012). Due to its exceptional observed brightness, it has been targeted with previous works attempting to observe Lyα, C IV, and C III with the Keck Observatory (Schenker et al. 2012; Stark et al. 2015; Mainali et al. 2018) and a previous attempt with PdBI (Schaerer et al. 2015) to observe [C II], however, the observations did not result in a significant detection.

We present the successful spectroscopic confirmation of A1703-zD1 and constraints on the properties of the other two sources based on their non-detections. In Section 2, we describe the sample selection, observations and the findings from our line scans. In Section 3, we provide the properties of the sources and comparisons to the literature, and in Section 4, we give our summary and conclusions.

2 Sample selection, observations and line scans

We obtained NOEMA observations of three sources, A1703-zD1 (Bradley et al. 2012; Smit et al. 2014), EGS-5711424617 and EGS-1952445714 (hereafter EGS-5711 and EGS-1952 respectively; Smit et al. 2015). These galaxies were initially selected with the Lyman break technique as HST/F814W drop-out galaxies and subsequently identified as sources with blue Spitzer/IRAC [3.6] – [4.5] colours, implying high equivalent width [O III] + Hβ emission (Smit et al. 2014, 2015).

We obtained 1.2 mm observations using NOEMA in its most compact 10D configuration, with a single setup for each of the three sources, A1703-zD1, EGS-5711 and EGS-1952, approved in program W18FC. Using the datacubes we obtain after processing, we scan for prominent lines by collapsing channels in the range of 80 – 400 km s^{-1} (the range of expected [C II] line-widths). This optimises the width of the collapsed narrowband for which the strongest point-source signal within a 1 arcsec radius of the target source (identified in the HST-imaging) is found, if any. Scanning through the datacube also enables us to identify any lines present from serendipitous sources. We replicate this scanning in the sign-inverse of the datacube, to check if any noise is comparable to the signal detected from the target source and assess the robustness of any tentative (> 3σ) line detections.

Taking our NOEMA observations of A1703-zD1 in isolation we find a signal at 242.90 ± 0.01 GHz with S/N = 4.6, co-spatial with the lower bright clump and extended along the lensed arc, visible in HST imaging (See Figure 1). From previous observations by Schaerer et al. (2015), we independently identified a tentative detection of [C II] with S/N = 3.4 at 242.853 ± 0.009 GHz and we therefore combine both data-sets. To obtain an unresolved measurement of A1703-zD1 we taper the datacube to match the spatial extent of A1703-zD. From this we find a detection at 242.82 ± 0.01 GHz with an increase in the peak S/N to 6.1, yielding a best-fit $z_{[CII]} = 6.8269 \pm 0.0004$ from the extracted spectrum (See Figure 1). This higher S/N when matching the spatial extent of the target (and alignment with the rest-frame UV emission) is a clear confirmation of the detection. We therefore use the tapered

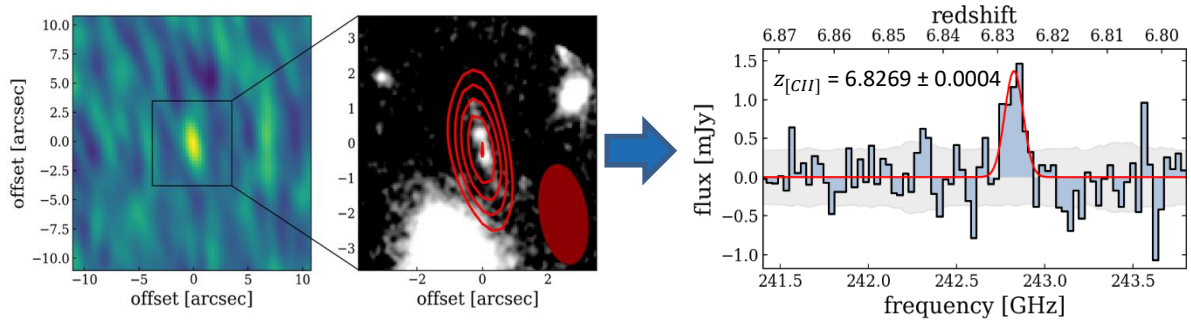

Fig 1. (Left) Collapsed NOEMA narrowband around the [C II] line in A1703-zD1. (Middle) Red contours showing the [CII] emission plotted over HST imaging. (Right) Spectra of the [CII] line with redshift.

imaging for our final measurements. We collapse the datacube over the frequency range 242.72 – 242.92 GHz and measure the total flux using 2D gaussian fitting from the routine imfit in the Common Astronomy Software Application (CASA).

3 SOURCE PROPERTIES

In the local universe we see a tight $L_{[CII]}$ – SFR relationship (De Looze et al. 2014; log SFR = – 6.99 + 1.01 × log [CII]). Recent studies of 'normal' (i.e. main sequence) star-forming galaxies with redshifts at $4.4 < z < 5.9$ and galaxies at $z \sim 6.5$ with high Lyα luminosities have also shown consistency with the local relation when including the dust-obscured SFR (e.g., Matthee et al. 2019; Schaerer et al. 2020). In contrast, a few studies have found that lensed galaxies with a lower SFR are more likely to be below the locally observed relation (e.g., Knudsen et al. 2016; Bradač et al. 2017). In particularly the strongest lensed object, MS0451-H (Knudsen et al. 2016), with the lowest intrinsic SFR shows the strongest deficit in $L_{[CII]}$. If confirmed, this could suggest differing ISM properties in faint, and possibly more metal poor, high-redshift galaxies. A1703-zD1 is a strongly lensed galaxy with a modest intrinsic SFR_{UV} of 6.7 ± 0.6 M yr^{-1}, but we find no evidence of a significant offset to the local relation, as A1703-zD1 lies below, but within 1σ, of the local $L_{[CII]}$ – SFR relation.

An important consideration in assessing a possible [C II] deficit is the potential for extended [C II] emission (e.g., Fujimoto et al. 2019, 2020) compared to the rest-frame UV data, in particular for sources with smearing due to strong gravitational lensing. This effect was recently studied by Carniani et al. (2020), who find that [C II] emission can be two times more extended than [O III]. In A1703-zD1, we aim to account for lens smearing by tapering the datacube to match the spatial extent of A1703-zD1 in the HST imaging, allowing us to obtain a more accurate flux measurement. Without tapering, we calculate a [C II] integrated flux value which is 51 per cent of our fiducial measurement. However, extended [C II] beyond the rest-frame UV could still be missed even with our current tapering strategy, consistent with Carniani et al. (2020).

We use the spatial extent of the [C II] detection to investigate the velocity structure of A1703-zD1 and identify a velocity gradient with a maximum projected velocity difference over the galaxy (Δv_{obs}) of 103 ± 22 km s^{-1}. Such a velocity gradient could be the signature of a rotating disk, or a merger of [C II] emitting galaxies. To determine the likelihood of a disk-like rotation we compare the projected velocity range of a galaxy with the velocity dispersion of the system using $\Delta v_{obs} / 2\sigma_{tot}$, where a ratio of > 0.4 indicates a likely rotation dominated system (Förster Schreiber et al. 2009). We find $\Delta v_{obs} / 2\sigma_{tot} = 0.79 \pm 0.23$ for A1703-zD1, which supports the interpretation of a possibly rotation dominated system. Bradley et al. (2012) find three distinct star-forming clumps with an extended linear morphology in the source-plane reconstruction of A1703-zD1. If we assume ordered circular rotation we can use the FWHM of [C II] to estimate the dynamical mass. We use $M_{dyn} = 1.16 \times 10^5 \, v_{cir}^2 \, D$ (Capak et al. 2015), where $v_{cir} = 1.763 \times \sigma_{[CII]} / \sin i$ in km s^{-1}, i is the disk inclination angle, and D is the disk diameter in kpc (we use D = 4 kpc found in Bradley et al. 2012; measured in the reconstructed sources-plane image). Assuming a viewing angle of 45 degrees we find $M_{dyn} = 12.1 \pm 4.8 \times 10^9 \, M_\odot$. The stellar mass of A1703-zD1 was esimated to be $0.7 \pm 0.1 \times 10^9 \, M_\odot$ (Bradley et al. 2012). This stellar mass is only ~ 6 per cent of the total dynamical mass that we measure. We note

that there are large uncertainties on the dynamical mass, as there is a large dependency on the viewing angle (which is unknown), however, the low ratio suggests that A1703-zD1 is a gas rich system

4 SUMMARY AND CONCLUSIONS

We have presented new NOEMA observations, scanning for the [C II]158μm line in three Lyman break galaxies with photometric redshifts at z = 6.6 − 6.9. Our main findings are as follows:

• We detect [C II] in one of our three sources, confirming the redshift at z = 6.8269 ± 0.0004 for the strongly lensed galaxy A1703- zD1 (6.1σ). Our non-detections are consistent with these being dust-poor galaxies with low [C II] luminosity.

• We carefully account for any extended emission of [C II] due to lens smearing in A1703-zD1 and find the [C II] luminosity to be consistent with, but slightly below, the local $L_{[CII]}$ – SFR relation.

• We see a velocity gradient across A1703-zD1, with a kinematic ratio that suggests a possible rotation dominated system, though higher resolution [C II] observations are needed to confirm this.

We have demonstrated the ability of NOEMA to search for [C II] in 'normal' star-forming galaxies at z > 6, complementing ALMA by observing EoR galaxies in the Northern Hemisphere. With the launch of JWST this capability will be particularly useful for rare, lensed sources and intrinsically luminous objects that will be discovered outside the limited JWST survey area using the next generation of large area surveys, such as the Euclid mission and the Rubin observatory.

REFERENCES

Bouwens R. J., et al., 2021, arXiv e-prints, p. arXiv:2106.13719
Bowler R. A. A., Bourne N., Dunlop J. S., et al., 2018, MNRAS, 481, 1631
Bradač M., et al., 2017, ApJ, 836, L2
Bradley L. D., et al., 2012, ApJ, 747, 3
Capak P. L., et al., 2015, Nature, 522, 455
Carniani S., et al., 2020, MNRAS, 499, 5136
De Looze I., et al., 2014, A&A, 568, A62
Endsley R., Stark D. P., Charlot S., et al., 2021, MNRAS, 502, 6044
Förster Schreiber N. M., et al., 2009, ApJ, 706, 1364
Fujimoto S., et al., 2019, ApJ, 887, 107
Fujimoto S., et al., 2020, ApJ, 900, 1
Ginolfi M., et al., 2020, A&A, 633, A90
Harikane Y., et al., 2019, ApJ, 883, 142
Hashimoto T., Inoue A. K., Tamura Y., et al., 2019, PASJ, 71, 109
Hodge J. A., da Cunha E., 2020, Royal Society Open Science, 7, 200556
Jung I., et al., 2020, ApJ, 904, 144
Kennicutt R. C., Evans N. J., 2012, ARA&A, 50, 531
Knudsen K. K., Richard J., Kneib J.-P., et al., 2016, MNRAS, 462, L6
Laporte N., Nakajima K., Ellis R. S., Zitrin A., Stark D. P., Mainali R.,
Roberts-Borsani G. W., 2017, ApJ, 851, 40
Mainali R., et al., 2018, MNRAS, 479, 1180
Matthee J., et al., 2019, ApJ, 881, 124
Schaerer D., Boone F., Zamojski M., et al., 2015, A&A, 574, A19
Schaerer D., et al., 2020, A&A, 643, A3
Schenker M. A., Stark D. P., Ellis R. S., et al., 2012, ApJ, 744, 179
Schouws S., et al., 2021, arXiv e-prints, p. arXiv:2105.12133
Smit R., et al., 2014, ApJ, 784, 58
Smit R., et al., 2015, ApJ, 801, 122
Stark D. P., 2016, ARA&A, 54, 761
Stark D. P., et al., 2015, MNRAS, 454, 1393

Kay Morrison

Postgraduate Researcher

School of Engineering

"Backward to move forward: the power of inverse order in forensic video enhancement."

Morrison, K.
School of Engineering, Liverpool John Moores University, 3 Byrom St, Liverpool L3 3AF
k.morrison@2019.ljmu.ac.uk

Abstract. Forensic video enhancement is a critical aspect of multimedia forensics, with applications in crime scene reconstruction or identification tasks. Despite its importance, there needs to be more consensus on the standard sequence for applying image enhancement techniques. This paper investigates the consequences of applying video enhancement filters in an incorrect order and highlights their negative impact on the final output. Factors affecting the feasibility of forensic video enhancement are discussed. The image generation model, a conceptual framework for analysing and processing visual evidence, is introduced, and its potential for guiding the optimal sequence of image enhancement filters is explored. The need for a universal image enhancement procedure that can be adapted to various scenarios, minimising the formation of undesirable distortions and adhering to forensic principles and best practices is emphasised.

Keywords. Video Forensics, Video Enhancement, Image Generation Model, Inverse Order

1. Introduction

In the realm of digital and multimedia forensics, image enhancement methods are frequently employed to assist with various forensic tasks, such as identifying license plates, faces, clothing and fingerprints, analysing what happened on the crime scene, and examining disputed documents (SWGDE, 2016). Often, multiple image-processing operations are applied concurrently to these images. Similar to a chain reaction, every processing operation applied to an image can have a significant impact on any future processing of the same image. Even when applying the same enhancement techniques with identical settings, applying them in incorrect sequence may lead to a loss in image fidelity or the creation of false features, including image noise or false edges. The goal of image enhancement is to improve the visual quality of an image for scientific investigations and legal purposes, making it more useful for analysis and interpretation (Siegel & Saukko, 2012; SWGDE, 2016). Nevertheless, the media forensics community has yet to reach a consensus on the standard sequence for applying image enhancements. As each enhancement case has distinct requirements, necessitating diverse combinations of image processing operations and settings and establishing a particular order of operations for image enhancement has been perceived as unfeasible. While video enhancement is not a novelty, the existing body of research has predominantly focused on specific methods and procedures rather than approaching the matter comprehensively from the standpoint of forensic science. This paper will provide examples of the consequences of utilising an incorrect order of video enhancement filters and highlight its negative impact on the final output. The future work will concentrate on developing a universal image enhancement procedure that can be seamlessly adapted to different scenarios, reduces the formation of undesirable distortions, and adheres to forensic principles and best practices.

2. Factors affecting the feasibility of forensic video enhancement.

The efficacy and success of forensic video enhancement is a complicated and multi-layered matter, given the broad spectrum of aspects that might affect it. In order to maximise the feasibility of the enhancement, a myriad of factors has to be thoroughly evaluated, and the methods must be modified in line with the specific objectives of the enhancement (Rao & Chen, 2012). The particular goal of the analysis is contingent upon the quality of the video image under analysis. It is essential to acknowledge that not all objectives may be attainable, and the nature of the visual data informs the outcome (Du & Ward, 2010). For instance, a lower-quality image may be adequate for discerning individual features such as gender or ethnicity of an individual. Whereas a higher-quality image is indispensable for capturing minute facial details for

identification purposes accurately. In contrast to the overall resolution of a video, the resolution of a region of interest (ROI) pertains to the number of pixels that make up the target of interest for enhancement rather than the overall resolution of the video. In specific applications, such as video analytics and surveillance, the ability to enhance the ROI is of paramount importance (Rao & Chen, 2012). For instance, high-definition (HD) footage capturing a remote vehicle may not be as valuable as low-resolution footage capturing a license plate in close proximity to the camera. The latter scenario provides a higher ROI resolution, enabling greater accuracy in identifying the license plate details. The success of the enhancement hugely depends on the compression level of the footage. This compression may manifest as spatial compression between pixels of the same frame or temporal compression between different frames. The compression process causes loss of detail, the introduction of artifacts and nonlinearities, and prediction mistakes (Mukhopadhyay, 2011; Gonzales & Woods, 2018). The frame rate, the number of frames and the position of the subject of interest within various frames are crucial variables in producing high-quality video outputs. Having multiple frames within footage vastly increases the likelihood of achieving a more favourable outcome than relying simply on a single still image (Mahalanobis, 2008; Li et al.., 2010). In addition, using multiple frames reduces noise, blurriness, and artifacts, thereby improving the quality and accuracy of the processed images (Ding et al., 2019). Ultimately, in video processing, the confluence of noise, blur, brightness, and colour distortions poses crucial challenges that significantly affect the overall quality (Rao & Chen, 2012).

3. Image generation model

The image generation model illustrates the manner in which light from a real-world scene is converted into a digital image or video that is eventually recorded as a string of binary numbers. This conceptual framework resembles blood detection and analysis in traditional forensic methods (Jerian, 2023). Both approaches involve the systematic and precise determination and evaluation of relevant evidence in order to produce admissible evidence for legal reasons. Technical limitations might emerge at each stage of the processing of the image, causing differences between the envisioned representation of reality and the actual image acquired.

4. Defects introduced at each stage

According to Martin Jerian (2023), the image generation model involves several phases. The first phase is the representation of the actual scene or event taking place in the physical world, which is captured by the camera optics and converted into a digital signal by the sensor. Examples of scene-related defects include pattern noise over a detail of interest, perspective distortion caused by an angled camera position, optical blur caused by long-distance atmospheric turbulence, and poor lighting conditions or excessive presence of light sources (Damjanovski, 2013). The second phase involves processes happening within a camera. This phase can be divided into four subcategories: optics, sensor, processing, and encoding. Optics can introduce various defects, including optical distortion, chromatic aberration, optical blur, motion blur, and loss of detail. Sensor-related defects arise from the conversion of analogue signals to digital, including brightness, contrast, and colour issues, noise, high or low saturation, level compression, low resolution, interlacing, and low frame rate (Jerian, 2013; Bernacki, 2019). The processing can introduce defects such as various artifacts and alterations from demosaicking, level compression, loss of detail, noise, and advanced processing. Eventually, defects introduced during the encoding phase include loss of detail, compression artifacts, interlacing, and wrong aspect ratio (Jerian, 2013). The third phase includes the transmission, multiplexing, and compression of the signal. In the data transmission subphase, information is conveyed from the imaging device to the storage system through either an analogue or digital connection. The storage system can be situated locally or within a cloud-based infrastructure. Due to the nature of analogue connections, random or pattern noise may arise from substandard cabling or external interferences. On the other hand, digital connections are primarily susceptible to transmission errors and packet loss, which can result in missing frames, distortions, or visual artifacts. The multiplexing subphase integrates signals from multiple cameras, encompassing audio, timestamps, and metadata, into a unified file or byte stream. However, multiplexing can result in reduced resolution, discarded frames for signal alternation, and

playback difficulties, particularly in proprietary formats, leading to artifacts, glitches, and absent frames. Finally, the encoding subphase may lead to artifacts and glitches, particularly in old VHS systems with issues such as scratches and misalignment (Russ, 2001; Damjanovski, 2013; Jerian, 2013). The final phase is the visualisation of the image, which requires supplementary procedures, such as acquisition, transformation, and playback. Video evidence acquisition is the first stage of the multimedia investigation. Various techniques can be employed to obtain the video, such as employing DVR export functions, conducting forensic analysis of the hard drive, obtaining screen capture, or performing analogue capture of the video signal. Nevertheless, the latter two approaches should be reserved for instances when all other alternatives have been exhausted. It may be necessary to convert from a proprietary format, which could give rise to challenges, including inaccurate aspect ratios or resolutions, compression artifacts, and detail loss, as well as the duplication or omission of frames and the degradation of file integrity and original metadata. During this playback subphase, the pivotal factor is the quality and settings of the equipment utilised for video display. Poor display and inadequate lighting conditions may seriously impair the depicted image quality.

5. Implementing the image generation model in practical applications.

The practical implementation of image generation models requires a methodical and scientifically grounded strategy for rectifying image defects. Conventionally, investigators prioritise addressing the most pressing issue. By concentrating on the most prominent concern, subsequent refinements can be implemented more efficiently, thus enhancing the entire visual content thoroughly. Although this tactic is viable during the preliminary triage phase, more suitable methods exist for conducting a meticulous forensic examination of an image. The image generation model offers a scientific framework for determining the optimal filters and sequence for ameliorating image defects. Fundamentally, this process involves reversing the order in which the defects were introduced. This concept can be easily comprehended through an analogy to solving a mathematical equation: to isolate a variable, one must apply inverse operations in the reverse order in which they were initially applied. Utilising this methodical approach, the image generation model offers a more robust and scientifically based technique for rectifying image defects.

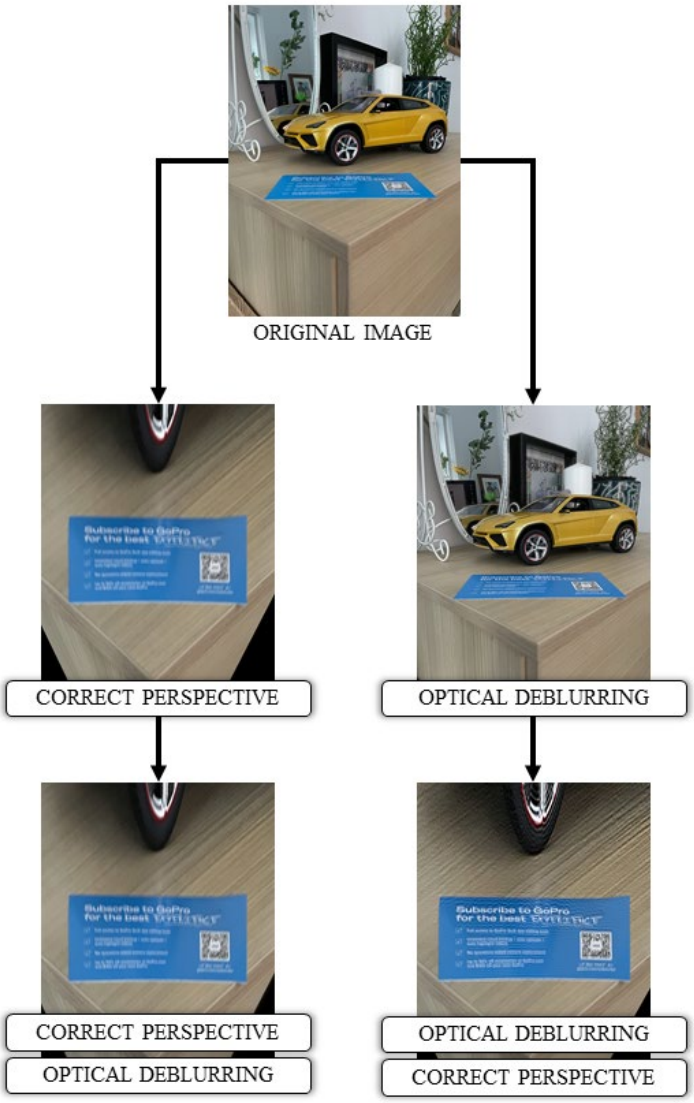

Figure 1: Comparison of image enhancement procedures using "correct perspective" and "optical deblurring" filters in AmpedFIVE Software. The figure demonstrates the results of two different filter sequences: the left side displays the image after first applying the "Correct Perspective" filter and subsequently the "Optical Deblurring" filter, while the right side presents the image after initially using the "Optical Deblurring" filter and then the "Correct Perspective" filter. The image on the right exhibits a notably superior clarity, underscoring the significance of employing the appropriate order of filters in forensic image enhancement.

6. The scientific basis of reversal in image enhancement

The process of reversing image enhancement is fundamentally rooted in mathematical principles, precisely the notion of inverse functions. In an ideal situation, the precise inverses of all functions associated with image defects would be known, allowing for accurate image restoration. However, practical applications of image enhancement techniques encounter challenges owing to the approximations inherent in mathematical models when depicting real-world phenomena, as they need to model the complex interactions between image features and defects precisely. For example, while enhancement software can effectively reduce the blurriness of an image, it cannot entirely restore the image to its pristine, pre-blur condition. This limitation highlights the need for a more refined and comprehensive mathematical framework to address real-world scenarios in image processing (Fontani, 2019).

7. Conclusion

The enhancement of forensic video is a complex procedure requiring a thorough assessment of various factors that can affect the accuracy and quality of the improved image. Forensic experts must use suitable video enhancement filters to guarantee that the resulting footage is admissible as legal evidence. The order in which these filters are utilised can vastly impact the overall efficiency of the enhancement process. Consequently, developing a universal framework to assist in choosing and applying the optimal filter sequence is essential for generating precise and dependable enhanced videos for legal use. Implementing image generation models in practical scenarios necessitates a methodical and scientifically founded approach to address image flaws. Contrary to conventional methods prioritising resolving the most prominent issues first, the image generation model offers a more resilient, science-driven technique by reversing the order of defect introduction.

8. Future work

Future research should be directed towards extending the current mathematical justification to encompass more realistic situations in image processing. Such an endeavour would involve the development of novel models and algorithms that can more accurately approximate the relationships between image features and defects.

9. References

1. Bernacki, J. (2019) “Digital Camera identification based on analysis of optical defects,” Multimedia Tools and Applications, 79(3-4), pp. 2945–2963.
2. Damjanovski, V. (2013) CCTV: From light to pixels. Amsterdam: Butterworth-Heinemann, an imprint of Elsevier.
3. Ding, Z., Yao, L., Lie, B. and Wu, J. (2019) Review of the application of ontology in the field of image object recognition. Proceedings of the 11th International Conference on Computer Modeling and Simulation.
4. Du, S. and Ward, R.K. (2010) Adaptive region-based image enhancement method for robust face recognition under variable illumination conditions. IEEE Transactions on Circuits and Systems for Video Technology, 20(9), pp. 1165–1175.
5. Fontani, M. (2020) Amped five filter order: It's better to get it right!, Amped Blog. Available at: https://blog.ampedsoftware.com/2019/07/11/amped-five-filter-order-its-better-to-get-it-right/ (Accessed: April 18, 2023).
6. Gonzalez, R.C. and Woods, R.E. (2018). Digital Image Processing, 3rd edition. Prentice Hall, New Jersey
7. Jerian, M. (2023) The Image Generation Model, Forensic Focus. Amped Blog. Available at: https://www.forensicfocus.com/news/the-image-generation-model/ (Accessed: April 18, 2023).
8. Li, X., Hu, y., Gao, X., Tao, D. and Ning, B. (2010) A multi-frame image super-resolution method. Signal Processing. 90(2), pp. 405–414.
9. Mahalanobis, A. (2008) Multi-frame Adaptive Object Recognition. SPIE Proceedings
10. Mukhopadhyay, J. (2011) Image and Video Processing in the Compressed Domain. Boca Raton, FL: Chapman & Hall/CRC.
11. Rao, Y. and Chen, L. (2012) A Survey of Video Enhancement Techniques. Journal of Information Hiding and Multimedia Signal Processing, 3(1), pp. 71–99.
12. Russ, J. C. (2001). Forensic uses of digital imaging. CRC Press.
13. Scientific Working Group on Digital Evidence. (2016) Section 11 Best Practices for Documenting Image Enhancement 9 (version 1.0). Available at: https://www.irisinvestigations.com/wp-content/uploads/2019/05/SWGDE-Image-Processing-Guidelines-020816.pdf [accessed on 15/4/2023]
14. Siegel JA and Saukko PJ. (2012) Encyclopedia of Forensic Sciences, Second Edition, Digital Evidence/Photography and Digital Imaging, Waltham: Academic Press, pp. 335–341

Bethan Williams

Postgraduate Researcher

Astrophysics Research Institute

Formation of stars and clusters in the extreme environment of the Galactic Centre

Bethan Williams[1]★, Steven Longmore[1] and Daniel Walker[2]
[1]*Astrophysics Research Institute, Liverpool John Moores University, IC2, 146 Brownlow Hill, Liverpool, L3 5RF, UK.*
[2]*Jodrell Bank Centre for Astrophysics, Department of Physics and Astronomy, University of Manchester, Oxford Road, Manchester M13 9PL, UK.*

★B.A.Williams@2015.ljmu.ac.uk

Abstract. Young massive clusters (YMCs) are compact (≤1 pc), high-mass (>10^4 $M_\odot$) stellar systems of significant scientific interest. Due to their rarity and rapid formation, we have very few examples of YMC progenitor gas clouds before star formation has begun. As a result, the initial conditions required for YMC formation are uncertain. Here, high-resolution ALMA observations and Mopra single-dish data are presented, showing that a cloud in the Galactic has the potential to become an Arches-like YMC (10^4 $M_\odot$, r ~ 1 pc), but is not yet forming stars. This would mean it is the youngest known pre-star forming massive cluster and therefore could be an ideal laboratory for studying the initial conditions of YMC formation. 96 low-mass sources were found in the dust continuum. The source separations are consistent with thermal fragmentation. It is not possible to unambiguously determine the dynamical state of most of the sources, as the uncertainty on virial parameter estimates is large. We find evidence for large-scale (~1 pc) converging gas flows, which could cause the cloud to grow rapidly. The highest density gas is found at the convergent point of the large-scale flows. We expect this cloud to form many high-mass stars but find no high-mass starless cores.

1. Introduction

Young massive clusters (YMCs) are gravitationally bound stellar systems with masses ≥10^4 $M_\odot$, radii ~1 pc, and ages ≤ 100 Myr (Portegies Zwart et al. 2010). They provide an important astrophysical laboratory for studying stellar evolution and dynamics. However, despite their importance, there are only limited observational examples of YMC progenitor clouds before star formation has begun (e.g., Ginsburg et al. 2012; Longmore et al. 2012). The two main proposed YMC formation mechanisms are the monolithic "in situ" mode and the hierarchical "conveyor belt" mode (Longmore et al. 2014). Differentiating between these mechanisms is difficult observationally, and a massive molecular cloud must be caught on the cusp of forming stars if we are to observe the very initial stages of YMC formation and determine which mechanism is dominant.

Such clouds have remained elusive in the Milky Way. The most promising examples to date have been in the Central Molecular Zone (CMZ), particularly in a region known as the 'dust ridge'. This 'dust ridge' contains a collection of six massive, compact, largely quiescent clouds. These clouds have frequently been identified as potential progenitors to YMCs (e.g., Walker et al. 2015; Barnes et al. 2019). The gas clouds studied most frequently are those with signs of ongoing star formation (e.g., Lu et al. 2019, 2020; Walker et al. 2021). Unfortunately, none of these clouds can be considered pre-star-forming. Therefore, in this report, attention is turned to the least studied of the dust ridge clouds, cloud 'd'. Despite having a similar mass and radius to other dust ridge clouds, this cloud shows no signs of star formation on larger scales. In this report, high resolution observations towards this cloud will be presented. Additionally, some early reports on a neighbouring cloud, cloud 'e', will be made. The aim of this report is to determine whether or not star formation is occurring at the scale of

individual cores and understand the fate of this cloud by investigating the gas density distribution in relation to large scale gas kinematics.

2. Data and Methodology

Data were taken using the Atacama Large Millimeter/submillimeter Array (ALMA). ALMA is an interferometer consisting of 66 radio telescopes, operating at wavelengths between 0.32 and 3.6 mm. Observations were made of dust ridge clouds using ALMA Band 6, which observes at a frequency of ~230 GHz (1.3mm). Photometric and spectroscopic observations were both made.

2.1 Photometry

Observations were made of the dust continuum at ~230 GHz. The observations have an angular resolution of ~0.13″, allowing scales of 1000 au to be resolved at a distance of 8.4 kpc (Abuter et al. 2019). The continuum data was imaged using CASA Version 5.6.0.68 (McMullin et al. 2007) and CASA's `tclean` task was used to clean the continuum. The data suffer with an inherent limited flux recovery due to the incomplete *uv*-coverage of the interferometer. This was accounted for by combining the interferometric data with the most appropriate large-scale data. To recover the continuum emission, ~1″ resolution data from Barnes et al. (2019) was used, which combines observations from ALMA's 12m array and 7m array with BOLOCAM Galactic Plane Survey (BGPS, Ginsburg et al. 2013) data. This data was scaled (as the large-scale data was taken at a different frequency to the interferometric 0.13″ data) and then feathered into the 0.13″ data to recover the large-scale emission.

2.2 Spectroscopy

The observations contain 7 spectral windows, 5 of which targeted specific molecular transitions in the lower sideband with a spectral resolution of ~0.77 kms^{-1}. The remaining two spectral windows were dedicated to broad-band continuum detection in the upper sideband, with a spectral resolution of ~2.5 kms^{-1}. The target spectral lines were split out using CASA's `split` task and then the continuum subtracted from them using the `uvcontsub` task. Finally, the lines were cleaned using the `tclean` task. Only the 12m data is available for the spectral lines, and so the large-scale structure is lost.

3. Results

2.1 Photometry

Using dendrogram analysis (e.g., Rosolowsky et al. 2008), 96 structures were found above a 3σ level, and only nine sources found above a 5σ level in cloud 'd' (Figure 1). By extracting the fluxes of each structure, the mass can be calculated. The effective radius of each structure was also calculated by calculating the radius of a circular source with an area equal to that of the structure ($R_{\rm eff} = \sqrt{A/\pi}$, where A is the area enclosed within the dendrogram boundary). Based on a dust temperature of 20 K, the mean mass, radius and number density of the 96 compact continuum sources are 0.67 $M_\odot$, ~1.6 × 10^3 au and 7.1 × 10^6 cm^{-3} respectively, all computed from within the footprint of the dendrogram leaf. The total combined mass of the sources is 65 $M_\odot$.

Using the continuum, nearest neighbour analysis was also carried out. From this, a mean separation of ~1.5 × 10^4 au was found between structures in cloud 'd'. Using a range of temperatures (20 – 40 K) and mass and radius estimates for this section of cloud 'd' from Walker et al. (2018), both thermal and turbulent Jeans length estimates were calculated. For the thermal Jeans length, estimates of $\lambda_{\rm J,therm} = 8.0^{+4.2}_{-3.4}$ × 10^3 au were found. Estimates for the turbulent Jeans length are in the range $\lambda_{\rm J,turb} = 5.3^{+1.6}_{-1.6}$ × 10^4 au. Figure 2 shows the distribution of the separations, along with the mean value (black dashed line) and the ranges of the thermal and turbulent fragmentation lengths (shaded regions). The mean separation of 1.5 × 10^4 au lies between these ranges, meaning it is potentially consistent with both, although marginally more consistent with thermal Jeans fragmentation.

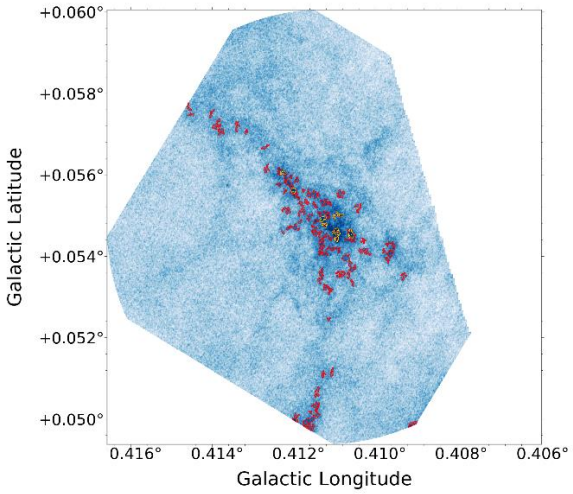

Figure 1: Locations of leaves extracted using dendrogram analysis. The dendrogram was computed using a threshold of 3σ (σ = 16μJy), an increment of σ and an Npix value of 77. Red contours show the individual compact continuum sources ('leaves') isolated by the dendrogram, of which 96 are found. Yellow contours show the nine continuum sources detected above 5σ.

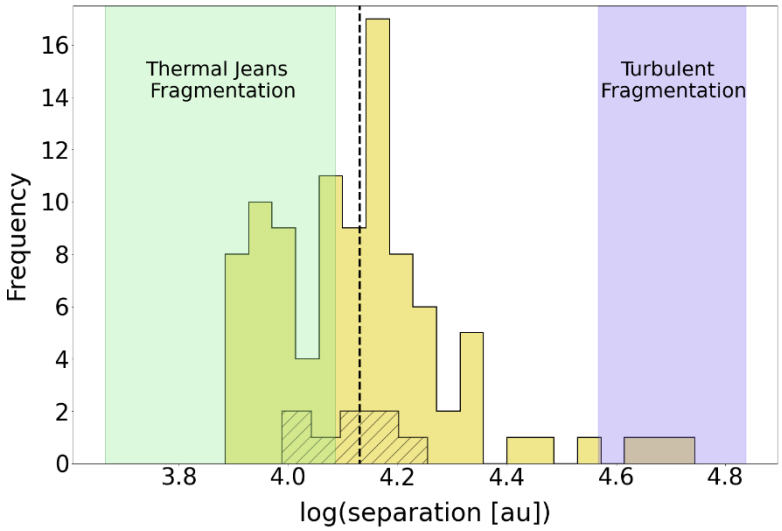

Figure 2: The separations of the 96 individual continuum sources. The black hatched histogram shows the same quantity for the nine 5σ sources. The black dashed line shows the mean separation. The green shaded region represents the range of predicted thermal Jeans lengths and the blue shaded region represents the range of predicted turbulent Jeans lengths.

The same analysis has been performed for cloud 'e' and a total of 20 structures found above a 5σ level. Mean mass estimates are in the range 6 – 17 $M_{\odot}$. However, not much more can be reported on this as the work is still unpublished.

2.2 Spectroscopy

^{13}CO, CH_3CN and SiO was searched for towards the cloud 'd' continuum sources. ^{13}CO and SiO are both tracers of outflows and CH_3CN is a tracer of hot protostellar cores. No CH_3CN emission is detected towards the continuum sources, nor are any SiO outflows identified. ^{13}CO is detected but is widespread and does not appear to show any distinct outflow morphology. Therefore, cloud 'd' remains unique among the dust ridge clouds in still having no signs of star formation.

As well as these molecular lines, three transitions of formaldehyde (H_2CO) were also targeted. H_2CO effectively traces the dust. The lowest energy H_2CO transition was used to perform virial analysis on the cloud 'd' continuum sources. Of the 96 sources, only 13 have clearly detected spectra. Using the

velocity dispersions obtained from these spectra, a virial parameter could be calculated for each of the 13 sources. Virial parameters were found in the range $5^{+13}_{-4.94}$ - 45^{+55}_{-33}. Generally, a virial parameter of $\alpha \leq 2$ indicates that a body is gravitationally bound. Therefore, it seems as though most of the sources in cloud 'd' are not gravitationally bound, although the uncertainty on the values means that some sources may be.

Similar analysis has again, been performed for cloud 'e'. In cloud 'e' there are signs of star formation, and some sources are gravitationally bound. However, once again, as this work is currently unpublished, not much more can be reported.

Large scale molecular line observations from the MALT90 survey (Foster et al. 2011, 2013; Jackson et al. 2013) show gas motions across cloud 'd'. Figure 3 shows the motions of HNCO. Analysis of these images show that cloud 'd' appears to be at a convergent point of these gas flows. The time it will take for mass to converge on this point is of the order 10^5 years, meaning that star formation could be imminent at this point.

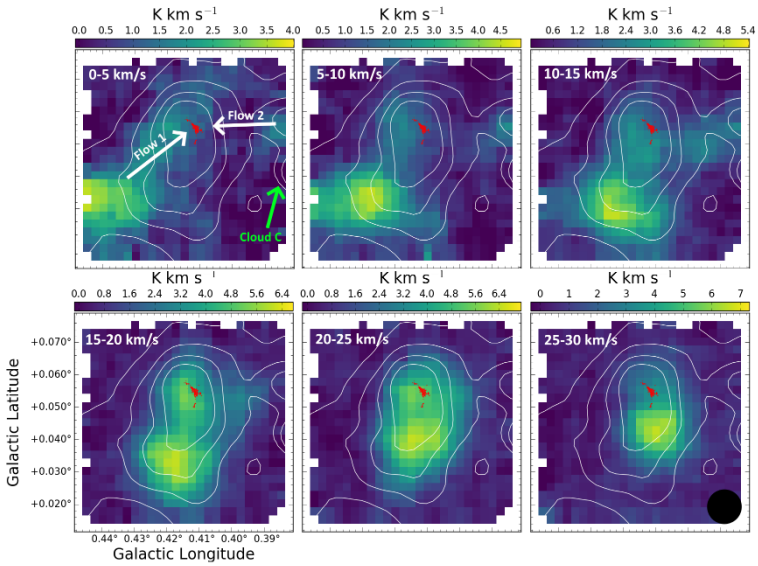

Figure 3: HNCO data of cloud 'd' from the MALT90 survey. Red contours show the 0.13″ ALMA data.

4. Summary and Conclusions

Summarising the results for cloud 'd':

- This region of cloud 'd' contains low mass structures, separated on scales of ~10^4 au.
- The projected separations have a tendency towards predicted thermal Jeans length.
- None of the identified structures show signs of star formation. As star formation has been detected in a similar CMZ cloud using an identical observational setup (Walker et al. 2021), it is fair to conclude that cloud 'd' is not currently forming stars.
- Virial analysis suggests that these structures are not likely to be gravitationally bound.
- Large-scale molecular line data suggests that cloud 'd' is at a point of convergence between of larger scale gas flows.

From these findings, the conclusion can be made that cloud 'd' is the earliest known pre-star forming massive cluster and is therefore an ideal laboratory in which to study the initial conditions of star and cluster formation in extreme environments. Ongoing work on neighbouring dust ridge cloud 'e' provides insight into a later evolutionary stage of cluster formation, as this cloud is already showing signs of star formation. Combining this with the study of cloud 'd' and similar clouds, we begin to expand our knowledge of star forming relations in extreme (but cosmologically typical) conditions and therefore can increase our understanding of a fundamental pillar of astrophysics.

Bibliography

Abuter, R. et al., 2019. A geometric distance measurement to the Galactic center black hole with 0.3\% uncertainty. *Astronomy & Astrophysics,* Volume 625, p. L10.

Barnes, A. T. et al., 2019. Young massive star cluster formation in the Galactic Centre is driven by global gravitational collapse of high-mass molecular clouds. *Monthly Notices of the Royal Astronomical Society,* 486(1), pp. 283-303.

Foster, J. B. et al., 2011. The Millimeter Astronomy Legacy Team 90 GHz (MALT90) Pilot Survey. *The Astrophysical Journal Supplement Series,* 197(2), p. 25.

Foster, J. B. et al., 2013. Characterisation of the MALT90 Survey and the Mopra Telescope at 90 GHz. *Publications of the Astronomical Society of Australia,* Volume 30, p. e038.

Ginsburg, A., Bressert, E., Bally, J. & Battersby, C., 2012. There are No Starless Massive Proto-clusters in the First Quadrant of the Galaxy. *The Astrophysical Journal Letters,* Volume 758, p. L29.

Ginsburg, A. et al., n.d. The Bolocam Galactic Plane Survey. IX. Data Release 2 and Outer Galaxy Extension. *The A.*

Jackson, J. M. et al., 2013. MALT90: The Millimetre Astronomy Legacy Team 90 GHz Survey. *Publications of the Astronomical Society of Australia,* Volume 30, p. e057.

Longmore, S. N. et al., 2014. *The Formation and Early Evolution of Young Massive Clusters.* Heidelberg, s.n.

Longmore, S. N. et al., 2012. G0.253 + 0.016: A Molecular Cloud Progenitor of an Arches-like Cluster. *The Astrophysical Journal,* 746(2), p. 117.

Lu, X. et al., n.d. ALMA Observations of Massive Clouds in the Central Molecular Zone: Jeans Fragmentation and Cluster Formation. *The Astrophysical Journal Letters.*

Lu, X. et al., 2019. A Census of Early-phase High-mass Star Formation in the Central Molecular Zone. *The Astrophysical Journal Supplement Series,* 244(2), p. 35.

McMullin, J. P. et al., 2007. *Astronomical Data Analysis Software and Systems XVI.* San Francisco, Astron. Soc. Pac..

Rosolowsky, E. W., Pineda, J. E., Kauffmann, J. & Goodman, A. A., 2008. Structural Analysis of Molecular Clouds: Dendrograms. *The Astrophysical Journal,* 679(2), pp. 1338-1351.

Walker, D. L. et al., 2021. Star formation in 'the Brick': ALMA reveals an active protocluster in the Galactic centre cloud G0.253+0.016. *Monthly Notices of the Royal Astronomical Society,* 503(1), pp. 77-95.

Walker, D. L. et al., 2015. Tracing the conversion of gas into stars in Young Massive Cluster Progenitors. *Monthly Notices of the Royal Astronomical Society,* 449(1), pp. 715-725.

Walker, D. L. et al., 2018. Star formation in a high-pressure environment: An SMA view of the Galactic Centre dust ridge. *Monthly Notices of the Royal Astronomical Society,* 474(2), pp. 2373-2388.

Zwart, S. F. P., McMillan, S. L. W. & Gieles, M., 2010. Young Massive Star Clusters. *Annual Review of Astronomy and Astrophysics,* Volume 48, pp. 431-493.